

1 **Profiling of fine- and coarse-mode particles with LIRIC (Lidar /Radiometer Inversion**
2 **Code)**

3
4 M. R. Perrone¹, P. Burlizzi¹, F. De Tomasi¹, A. Chaikovsky²

5
6 ¹Mathematical and Physical Department, Universita' del Salento, 73100 Lecce, Italy

7 ²Institute of Physics, National Academy of Science, Minsk, Belarus

8
9 **Abstract**

10
11 The paper investigates numerical procedures that allow determining the dependence on altitude
12 of aerosol properties from multi wavelength elastic lidar signals. In particular, the potential of
13 the Lidar/Radiometer Inversion Code (LIRIC) to retrieve ~~the~~ vertical profiles of fine and
14 coarse-mode particles by combining ~~3-wavelength~~ lidar measurements [at 355, 532 and 1064](#)
15 [nm.](#) and collocated AERONET (AErosol RObotic NETwork) sun/sky photometer
16 measurements is investigated. ~~The used lidar signals are at 355, 532 and 1064 nm.~~ Aerosol
17 extinction coefficient (α_L), lidar ratio (LR_L), and Ångstrom exponent (Å_L) profiles from LIRIC
18 are compared with the corresponding profiles (α , LR, and Å) ~~retrieved~~ from a Constrained
19 Iterative Inversion (CII) procedure to investigate the LIRIC retrieval ability. Then, a [graphical](#)
20 ~~n~~-aerosol classification framework which relies ~~on the use of a graphical framework and~~ on the
21 combined analysis of the Ångstrom exponent (at the 355 and 1064 nm wavelength pair, $\text{Å}(355,$
22 $1064)$) and its spectral curvature ($\Delta\text{Å}=\text{Å}(355, 532)-\text{Å}(532, 1064)$) is used to investigate the
23 ability of LIRIC to retrieve vertical profiles of fine- and coarse-mode particles. ~~The $\text{Å}-\Delta\text{Å}$~~
24 ~~aerosol classification framework allows estimating the dependence on altitude of the aerosol~~
25 ~~fine modal radius and of the fine mode contribution to the whole aerosol optical thickness, as~~
26 ~~discussed in Perrone and co authors (2014).~~ The application of LIRIC to three different aerosol
27 scenarios dealing with aerosol properties dependent on altitude has revealed that the
28 differences between α_L and α vary with the altitude and on average increase with the decrease
29 of the lidar signal wavelength. It has also been found that the differences between Å_L and
30 corresponding Å values vary with the altitude and the wavelength pair, ~~since:~~ ~~t~~The sensitivity
31 of ~~Ångstrom exponents~~ to the aerosol size distribution ~~depends on which vary with~~ the
32 wavelength pair ~~was responsible for these last results.~~ ~~The aerosol classification framework has~~
33 ~~revealed~~ ~~It is shown either~~ that the observed deviations ~~between LIRIC and the corresponding~~
34 ~~CII procedure retrieval products~~ are due to the ~~fact that~~ LIRIC constrain that fine- and

1 ~~coarse does not allow to the~~ modal radius are height independent, and that the constrain of
2 ~~fine mode particles to vary with the altitude. It is shown that this~~ represents the main source of
3 uncertainties in LIRIC results. ~~The plot on the graphical framework of the Å-Å data points~~
4 ~~retrieved from the CH procedure has indicated that the fine mode particle modal radius can~~
5 ~~vary with altitude when particles from different sources and/or from different advection routes~~
6 ~~contribute to the aerosol load. Analytical back trajectories combined with linear particle~~
7 ~~depolarization ratio profiles from lidar measurements at 355 nm and dust concentrations from~~
8 ~~the Barcelona Supercomputing Center Dust Regional Atmospheric Model (BSC-DREAM)~~
9 ~~have been used to demonstrate the dependence on altitude of the aerosol properties.~~

10

1 1 Introduction

2

3 The impact of aerosol on climate is widely recognized and several efforts have been
4 undertaken in the last years to characterize aerosol optical and microphysical properties and
5 estimate aerosol direct and indirect radiative effects. Ground and satellite based remote sensing
6 techniques have been developed to characterize aerosol properties from the ground up to the
7 top of the atmosphere. Satellite-based observations provide global monitoring of the aerosol
8 properties. On the contrary, ground-based observations are punctual but, they can allow a more
9 detailed and accurate characterization of the aerosol optical and microphysical properties.
10 Ground-based networks with similar remote-sensing devices and standardized data processing
11 procedures have been developed to partially overcome the local nature of ground-based
12 observations. The AEROSOL ROBOTIC NETWORK (AERONET, Holben et al., 1998) and the
13 European Aerosol Research LIDAR NETWORK (EARLINET, Matthias et al., 2004) represent two
14 typical examples. AERONET is a network of sun/sky photometers coordinated by NASA,
15 operating on global scale. Column-integrated aerosol optical and microphysical properties are
16 retrieved from AERONET sun/sky photometer observations (Dubovik and King, 2000;
17 Dubovik et al., 2006 and references therein). EARLINET is the European aerosol lidar
18 network, established in 2000, with the main goal of deriving long time series of the aerosol
19 vertical distribution and providing a comprehensive, quantitative, and statistically significant
20 data base for the aerosol distribution over Europe. Lidars represent nowadays the best devices
21 to retrieve aerosol vertical profiles. Aerosol effects on climate depend on the vertical
22 distribution of the aerosol optical and microphysical properties (e.g. [Seinfeld and Pandis, 1998](#);
23 Perrone et al., 2012). As a consequence, several numerical approaches have been developed to
24 invert aerosol extinction (α) and backscatter (β) coefficients retrieved from lidar measurements
25 at multiple wavelengths to particle parameters (Veselovskii et al., 2010; Veselovskii et al.,
26 2012; Müller et al., 2013 and references therein): the higher the number of the input parameters
27 the greater the number and the accuracy of the aerosol optical and microphysical properties
28 that are derived. Multi-wavelength Raman lidars equipped with a depolarization (δ) channel
29 are nowadays the most advanced lidar systems since they are generally equipped with
30 $(3\beta+2\alpha+1\delta)$ optical channels, as required in some advanced inversion procedures of lidar
31 signals (e.g. Müller et al., 2013). However, most Raman lidars are designed for night time

1 operation and they can only provide elastic lidar signals during daytime, as the lidar system
2 used in this study (e.g. De Tomasi et al., 2006). In addition, it would be highly desirable to
3 reduce the number of optical channels in some lidar experiments. Therefore, numerical
4 procedures only based on elastic lidar signals have been developed to characterize the
5 dependence on altitude of aerosol properties. Ansmann et al. (2012) have proposed the single-
6 wavelength POLIPHON (POLarization LIdar PHOtometer Networking) technique for the
7 retrieval of volume and mass concentration profiles for fine and coarse mode particles. This
8 method is based on the measured height profile of the particle depolarization ratio to separate
9 coarse dust from the residual aerosol particles (Wagner et al., 2013). A method which relies on
10 the use of a graphical framework and on the combined analysis of the Angstrom exponent (at
11 the 355 and 1064 nm wavelength pair, $\text{\AA}(355, 1064)$) and its spectral curvature ($\Delta\text{\AA}=\text{\AA}(355,$
12 $532)-\text{\AA}(532, 1064)$), calculated from the lidar extinction profiles at 355, 532, and 1064 nm,
13 respectively, has recently been used by Perrone et al., (2014) to estimate the dependence on
14 altitude of the aerosol fine mode radius (R_f) and of the fine mode contribution (η) to the aerosol
15 optical thickness (AOT). This method is denoted as $\text{\AA}-\Delta\text{\AA}$ graphical method. Chaikovsky et al.
16 (2012) have developed a numerical tool (LIRIC, LIdar/Radiometer Inversion Code) to retrieve
17 vertically resolved aerosol microphysical properties by combining backscatter coefficient
18 measurements at 3 wavelengths and sun/sky radiance measurements. This activity has been
19 performed in the frame of the European Project Aerosol, Clouds, and Trace gases Research
20 InfraStructure Network (ACTRIS, <http://www.actris.net/>) with the main aim of integrating
21 sun/sky photometer and lidar measurements from AERONET and EARLINET, respectively.
22 The GARRLiC (Generalized Aerosol Retrieval from Radiometer and Lidar Combined data)
23 approach recently proposed by Lopatin et al. (2013) pursues even deeper synergy of lidar and
24 radiometer data in the retrievals. Wagner et al. (2013) have recently evaluated the LIRIC
25 performance to determine microphysical properties of volcanic and desert dust. To this end,
26 LIRIC profiles of particle mass concentrations for the coarse-mode as well as for the non-
27 spherical particle fraction have been compared with results for the non-spherical particle
28 fraction from the POLIPHON method. The LIRIC spheroidal-particle model was considered as
29 main source of uncertainties in the LIRIC results.
30 The main goal of this study is to contribute to the characterization and development of
31 numerical procedures based on multi wavelength elastic lidar signals, to characterize the

1 dependence on altitude of aerosol properties, since most of the multi wavelength lidar systems
2 can only provide elastic lidar signals during the daytime operation. To this end, the potential of
3 LIRIC to retrieve vertical profiles of fine- and coarse-mode particle volume concentrations by
4 combining AERONET sun/sky photometer aerosol products and collocated in space and time
5 3-wavelength elastic lidar signals is investigated in this paper. More specifically, lidar
6 measurements at 355, 532 and 1064 nm and sun/sky radiometer measurements performed at
7 the Mathematics and Physics Department of Universita' del Salento, in south eastern Italy are
8 used in this study. Aerosol from continental Europe, the Atlantic, northern Africa, and the
9 Mediterranean Sea are often advected over south eastern Italy and as a consequence, mixed
10 advection patterns leading to aerosol properties varying with altitude are dominant (e.g.
11 Perrone et al., 2014). Three study cases representative of aerosol loads affected by different
12 sources are analyzed to test the LIRIC retrieval ability. To this end, extinction, lidar ratio, and
13 Angstrom coefficient profiles from LIRIC are first compared with the corresponding profiles
14 retrieved from a constrained iterative inversion procedure (Perrone et al., 2014). Then, the Å-
15 $\Delta\text{Å}$ graphical method (Perrone et al., 2014) is used to evaluate the potential of LIRIC to
16 retrieve vertical profiles of fine- and coarse-mode particle volume concentrations and to
17 understand the differences between LIRIC and the retrievals from the constrained iterative
18 inversion (CII) procedure. Depolarization lidar measurements at 355 nm, analytical
19 backtrajectories, and dust concentrations from the BSC-DREAM model
20 (<http://www.bsc.es/earth-sciences/mineral-dust-forecast-system/bsc-dream8b-forecast/north->
21 [africa-europe-and-middle-ea-0](http://www.bsc.es/earth-sciences/mineral-dust-forecast-system/bsc-dream8b-forecast/north-africa-europe-and-middle-ea-0)) are used to understand/support the change with altitude of the
22 aerosol fine modal radius and of the fine mode fraction resulting from the Å- $\Delta\text{Å}$ graphical
23 method. A short overview of LIRIC, the 3 wavelength lidar system, the constrained iterative
24 inversion procedure, and the Å- $\Delta\text{Å}$ graphical method is given in Section 2. Results are
25 presented and discussed in detail in Section 3. Summary and conclusion are given in Section 4.

26

27 **2 Methods**

28

29 **2.1 The LIRIC tool**

30

1 The basic structure of LIRIC is presented and discussed in Chaikovsky et al. (2012) and
2 Wagner et al. (2013). A short overview of LIRIC features is reported in this section.
3 AERONET inversion products and collocated background-corrected, elastically-backscattered,
4 lidar signals $P(\lambda_i, z)$ at three different wavelengths λ_i and at the altitude z represent the input
5 data set for LIRIC. More specifically, LIRIC has been designed for the analysis of the lidar
6 signals at 355, 532, and 1064 nm in the simplified retrieval mode which allows retrieving two
7 aerosol modes: fine and coarse. If polarization lidar measurements at 532 nm are also available
8 LIRIC can operate in the polarimetric mode, which allows retrieving three aerosol modes: fine,
9 coarse spherical and coarse spheroid. The LIRIC simplified retrieval mode is used in this study
10 since polarization lidar measurements at 532 nm are not available. The minimum measurement
11 height z_0 which depends on the lidar field of view and the lidar signal reference-height z_f must
12 also be provided. Note that from the ground up to $z = z_0$, LIRIC assumes constant aerosol
13 optical and microphysical properties and hence, height-independent particle backscatter and
14 extinction coefficients. LIRIC searches ~~the concentration for particle lidar~~ profiles that best
15 match the multi wavelength lidar measurements. It is also required that the integral of the
16 retrieved concentrations matches the AERONET-derived column volume concentrations to
17 retrieve the vertical profiles of fine $C_f(\lambda_i, z)$ and coarse $C_c(\lambda_i, z)$ particle volume concentrations
18 and the height-independent volume-specific backscatter $b_m(\lambda_i)$ and extinction $a_m(\lambda_i)$
19 coefficients of the fine (m=f) and coarse (m=c) mode. The least-square method (LSM) for the
20 statistically optimized inversion of multi-source data is used in LIRIC (Dubovik and King,
21 2000; Dubovik, 2004). The method requires covariance matrices of the lidar signal
22 measurement errors as a function of the height z (Wagner et al., 2013). The lidar signal
23 dispersion is calculated as a value for the measurement error at λ_i and z . Sixty thousand lidar
24 signals collected over about 30 minutes to increase the signal-to-noise ratio are used in this
25 study for each LIRIC run. Then, the standard deviation $\sigma_{\lambda_i}(z)$ is calculated from LIRIC to
26 estimate the dispersion and hence, the errors of the input lidar signals. The root mean square
27 (RMS) value of the standard deviation $\sigma_{\lambda_i}(z)$ taken all over the lidar signal altitude-range
28 ($\text{RMS}-\sigma_{\lambda_i}$) is calculated to obtain a mean column estimate of the dispersion of the input lidar
29 signals at λ_i . The residuals $\rho_{\lambda_i}(z)$ between the observed lidar signal values and the
30 corresponding ones calculated from LIRIC are minimized to retrieve fine and coarse particle
31 volume concentration profiles of good accuracy. To this end, the lidar input parameters z_0 and

1 z_f , and the regularization parameter sets are varied. We decided to calculate the root mean
 2 square value of the residuals taken all over the lidar signals altitude-range (RMS- ρ_{λ_i}), to obtain
 3 a mean estimate of the LIRIC retrieval accuracy at each wavelength λ_i : the smaller is the
 4 RMS- ρ_{λ_i} value the higher is the retrieval accuracy. Hence, for each set of input lidar signals,
 5 several runs have been performed to minimize RMS- ρ_{λ_i} by varying realistic z_0 , z_f , and
 6 regularization parameter values. Then, we have required that only the LIRIC outputs satisfying
 7 the following condition

$$8 \quad \text{RMS-}\rho_{\lambda_i} \leq 2 \times \text{RMS-}\sigma_{\lambda_i} \quad (1)$$

10 at 355, 532 and 1064 nm, respectively, could be considered of good-accuracy. More than 20
 11 LIRIC outputs satisfying condition (1) have commonly been used in this study to calculate the
 12 mean fine $C_{f,a}(\lambda_i, z)$ and coarse $C_{c,a}(\lambda_i, z)$ particle volume concentration ~~profiles. The $C_{f,a}(\lambda_i, z)$~~
 13 ~~and $C_{c,a}(\lambda_i, z)$ uncertainties have been set equal to ± 1 with corresponding~~ standard deviations
 14 (SDs) of the ~~corresponding~~ mean value. We know that we could use a different procedure than
 15 the above mentioned to calculate $C_{f,a}(\lambda_i, z)$ and $C_{c,a}(\lambda_i, z)$ mean values and corresponding
 16 standard deviations. However, we believe that the ~~used procedure indicated one can be~~
 17 ~~considered as satisfactory to go too well.~~ Aerosol extinction and backscatter coefficients from
 18 LIRIC, $\beta_L(\lambda_i, z)$ and $\alpha_L(\lambda_i, z)$, respectively, are defined as

$$19 \quad \alpha_L(\lambda_i, z) = C_f(\lambda_i, z) a_f(\lambda_i) + C_c(\lambda_i, z) a_c(\lambda_i) \quad (2)$$

$$21 \quad \beta_L(\lambda_i, z) = C_f(\lambda_i, z) b_f(\lambda_i) + C_c(\lambda_i, z) b_c(\lambda_i) \quad (3)$$

22
 23 For each set of lidar data, ~~the~~ mean extinction and backscatter ~~coefficients with corresponding~~
 24 ~~SDs profile arcs~~ are calculated by averaging all $\alpha_L(\lambda_i, z)$ and $\beta_L(\lambda_i, z)$ profiles, respectively
 25 determined by the LIRIC outputs satisfying condition (1). ~~$\alpha_L(\lambda_i, z)$ and $\beta_L(\lambda_i, z)$ uncertainties~~
 26 ~~are set equal to ± 1 SD of the corresponding mean value.~~ The aerosol extinction-to-backscatter
 27 ratio (also referred to as the aerosol Lidar Ratio, LR) and the fine mode fraction η_L at different
 28 wavelengths are computed as follows:

$$29 \quad \text{LR}_L(\lambda_i, z) = \alpha_L(\lambda_i, z) / \beta_L(\lambda_i, z) \quad (4)$$

1
$$\eta_L(\lambda_i, z) = \alpha_{L,f}(\lambda_i, z) / \alpha_L(\lambda_i, z) \quad (5)$$

2 where

3
$$\alpha_{L,f}(\lambda_i, z) = C_f(\lambda_i, z) a_f(\lambda_i) \quad (6)$$

4

5 Ångstrom exponent profiles for different wavelength pairs are computed in accordance with
6 the following relationship:

7

8
$$\mathring{A}_L(\lambda_1, \lambda_2, z) = - \{ \ln[\alpha_L(\lambda_1, z) / \alpha_L(\lambda_2, z)] \} / [\ln(\lambda_1 / \lambda_2)] \quad (7)$$

9

10 For each input data set, mean lidar ratio, fine mode fraction and Ångström exponent profiles
11 are calculated by averaging the $LR_L(\lambda_i, z)$, $\eta_L(\lambda_i, z)$ and $\mathring{A}_L(\lambda_1, \lambda_2, z)$ profiles determined by the
12 LIRIC outputs satisfying condition (1). Uncertainties are set equal to ± 1 SD of the
13 corresponding mean values.

14

15 **2.2 The 3-wavelength UNILE lidar system**

16

17 The ground-based lidar system at the Mathematics and Physics Department of Università' del
18 Salento (Lecce, 40.33°N; 18.11°E), that is used in this study and is identified as UNILE
19 (UNiversity of LEcce) lidar, operates within EARLINET since May 2000 (De Tomasi and
20 Perrone, 2003). It is nowadays composed by a 30 Hz Nd:YAG laser operating at its
21 fundamental wavelength, 1064 nm, and the second and third harmonic at 532 and 355 nm,
22 respectively. The backscattered radiation collected by the primary mirror of the Newton
23 telescope and collimated by a plane convex lens, is spectrally resolved by means of dichroic
24 mirrors and interferential filters. Then, the 1064 nm signal is detected by an avalanche
25 photodiode and an A/D transient recorder. The signal at 532 and 355 nm are detected by
26 photomultipliers connected to transient recorders that have both a 12 bit A/D conversion and a
27 photon counting (PC) capability. In this way the full dynamic range of the lidar signals can be
28 monitored. Transient recorders integrate over 2000 laser shots that correspond to about 60 s.
29 The lidar system is estimated to achieve full overlap between 0.5 – 1.0 km above the ground
30 level (a.g.l.). The UNILE lidar system was designed to derive elastically backscattered lidar

1 profiles at 355 nm, 532 nm and 1064 nm, respectively and the 355 nm-linear volume
2 depolarization ratio ($\delta(z)$) profile during day time measurements.

3

4 **2.3 Constrained iterative inversion procedure**

5

6 Aerosol extinction and backscatter coefficient profiles from LIRIC are compared with the
7 corresponding ones retrieved from a constrained iterative inversion (CII) procedure (Perrone et
8 al., 2014) to investigate the LIRIC method, as mentioned in the introduction. The constrained
9 iterative inversion procedure, whose main advantages and drawbacks are presented and
10 discussed in Perrone et al. (2014), is based on the assumption that the lidar ratio is constant
11 over the altitude. The LR constrain may represent a weak point of the CII procedure. A
12 sensitivity test on the impact of an altitude dependent LR on the CII procedure results is
13 provided in Perrone et al. 2014. The CII procedure ~~More specifically, it~~ allows determining
14 aerosol extinction ($\alpha(\lambda_i, z)$) and backscatter ($\beta(\lambda_i, z)$) coefficient profiles from 3-wavelength
15 lidar measurements by using as boundary conditions: (1) the AOT of a selected altitude range
16 and (2) the total backscatter coefficient β_T (due to molecules (β_M) and aerosol (β)) at a far-end
17 reference height z_f , and (3) by assuming that the aerosol optical microphysical properties are
18 constant from the ground up to $z = z_0$. Note that constrains (1)-(3) are also used by LIRIC and
19 that the AOTs at the lidar wavelengths are retrieved from collocated in space and time
20 AERONET measurements, as in LIRIC. The uncertainties of $\alpha(\lambda_i, z)$ and $\beta(\lambda_i, z)$ retrieved
21 from the constrained iterative procedure include statistical uncertainties due to the presence of
22 noise on the received lidar signals and systematic uncertainties as the ones due to the assumed
23 molecular profile, the reference backscatter ratio value, and the total measured AOT. As in
24 LIRIC, radiosonde measurements at the meteorological station of Brindisi
25 (<http://esrl.noaa.gov/raobs/>) that is 40 km north-west of the monitoring site of this study are
26 used to define the air density vertical profiles. Mean extinction and backscatter coefficient
27 profiles at each lidar wavelength are calculated by averaging a few thousand profiles generated
28 from the constrained iterative procedure by changing boundary conditions. The $\alpha(\lambda_i, z)$ and
29 $\beta(\lambda_i, z)$ uncertainties are set equal to one standard deviation of the mean value, respectively.
30 The vertical profiles of the Ångström exponents for different wavelength pairs are calculated in
31 accordance with Eq. 5. The spectral curvature $\Delta\tilde{A}(z)$ that is set equal to the difference

1
2

$$\Delta\mathring{A}(z) = \mathring{A}(355, 532, z) - \mathring{A}(532, 1064, z) \quad (8)$$

3 is also calculated. Ångstrom exponent and $\Delta\mathring{A}(z)$ profiles are calculated from the extinction
4 profiles at 355 nm, 532 nm, and 1064 nm generated by the implemented iterative procedure.
5 The mean profile of $\mathring{A}(\lambda_1, \lambda_2, z)$ and $\Delta\mathring{A}(z)$ is then calculated and the $\mathring{A}(\lambda_1, \lambda_2, z)$ and $\Delta\mathring{A}(z)$
6 uncertainties are set equal to one standard deviation of the corresponding mean values.
7 As mentioned, main boundary conditions used in the constrained iterative procedure are
8 common to LIRIC. However, the constrained iterative procedure searches for height-
9 independent lidar ratio (LR) values to satisfy the boundary conditions. By contrast, LIRIC uses
10 a typical algorithm for solving inverse problems and searches for concentration profiles of
11 aerosol modes invariant over the altitude that best match the AERONET column-integrated
12 fine- and coarse-mode particle volume concentrations and the measured lidar data. As a
13 consequence, aerosol extinction and backscatter coefficient profiles from LIRIC may differ
14 from the corresponding ones retrieved from the constrained iterative procedure if the modal
15 radii of the aerosol size distribution vary with z , as it will be shown in the following.

16

17 **2.4 Graphical framework for the aerosol classification**

18

19 The aerosol classification framework presented and discussed in Perrone et al. (2014) is used in
20 this study to investigate the potential of LIRIC to retrieve vertical profiles of fine- and coarse-
21 mode particle volume concentrations. The graphical classification framework allows to obtain
22 an estimate of the dependence on altitude of the aerosol fine modal radius ($R_{f,GF}$) and of the
23 fine mode contribution (η_{GF}) to the aerosol optical thickness at 532 nm from the spectral
24 curvature $\Delta\mathring{A}(z)$ versus the Ångstrom exponent $\mathring{A}(355, 1064, z)$ plot. Ångstrom exponents and
25 spectral curvature are calculated from extinction coefficient profiles retrieved at 355, 532, and
26 1064 nm, in accordance with Eqs. 7 and 8. Figure 1 (black lines) shows the aerosol
27 classification framework calculated by setting the real and imaginary refractive index value at
28 532 nm equal to 1.455 and 0.0047, respectively. The used n and k values are considered
29 representative of mixed aerosol types, in accordance with the discussion reported in Perrone et
30 al. (2014). Mie calculations of the aerosol spectral extinction for selected fine ($R_{f,GF} = 0.02,$
31 $0.05, 0.1, 0.15, 0.2, 0.3,$ and $0.4 \mu\text{m}$) and coarse ($R_{c,GF} = 0.5, 0.6, 0.7,$ and $0.8 \mu\text{m}$) modal radii,

1 combined in order to provide η_{GF} fractions at 532 nm of 1, 10, 30, 50, 70, 90, 99%, have been
2 performed to calculate the solid and dashed black lines of Fig.1, which represent the graphical
3 framework denoted as Mixed aerosol framework. Yellow solid and dashed lines in Fig. 1
4 represent the aerosol classification framework calculated by using the real and imaginary
5 refractive index values for dust recently reported by Wagner et al. (2012), which are $n = 1.55$
6 and $k = 0.008$ at 532 nm. It is denoted as Dust framework and allows to highlight the
7 sensitivity of the graphical framework to refractive index values. The dust refractive indices
8 were calculated from laboratory measurements on dust samples (Wagner et al., 2012). The test
9 shows that the average change in all the 49 grid points is of about 5%. The sensitivity of the
10 aerosol classification framework to changes in the coarse modal radii is revealed by the blue
11 graphical framework of Fig. 1 (Dust rev. coarse). It was obtained by increasing of 50% the
12 coarse modal radii ($R_{c,GF} = 0.75, 0.9, 1.05, \text{ and } 1.2 \mu\text{m}$) and by using the real and imaginary
13 refractive index values for dust from Wagner et al. (2012). The test shows that the graphical
14 framework moves on average downward as the coarse modal radii are increased of 50%. The
15 average change in all the 49 grid points with respect to the Mixed aerosol framework (Fig. 1,
16 black lines) is of about 4%. Effects of refractive index and coarse modal radius changes have
17 also been discussed in Gobbi et al. (2007). The Dust rev. coarse framework (Fig. 1, blue lines)
18 is best suited for aerosol loads heavily affected by dust particles.

19

20 **3. Results**

21

22 Three case studies are analyzed in this section to investigate the potential of LIRIC to retrieve
23 vertical profiles of fine and coarse-mode particles under different aerosol load scenarios. More
24 specifically, one case deals with aerosol measurements affected by anthropogenic, biomass-
25 burning, and soil particles. The second case deals with anthropogenic pollution affected by
26 marine aerosol and the last one deals with aerosols significantly affected by Sahara dust.

27

28 **3.1 Case study: August 29, 2011**

29

30 Results on lidar measurements performed on August 29, 2011 from 13:56 to 14:27 UTC are
31 first discussed in this section. Figure 2a shows the vertical profiles of the mean fine $C_{f,a}(\lambda_i, z)$

1 (black dotted line) and coarse $C_{c,d}(\lambda_i, z)$ (pink dotted line) particle volume concentration with
2 corresponding uncertainties (error bars) retrieved from LIRIC, in accordance with the
3 methodology described in Section 2.1. AERONET inversion products retrieved from sun/sky
4 photometer measurements (Lecce University) performed at 14.12 UTC have been used by
5 LIRIC. Figure 2a shows that fine and coarse particle volume concentrations are of the same
6 order of magnitude and vary similarly with the altitude. Atmospheric particle sizes on average
7 vary with source type and/or the pathways they have followed before reaching the monitoring
8 site. So, Fig. 2a indicates that particles from different sources and/or from different pathways
9 have contributed to the aerosol load and that the different contributions occurred almost at all
10 altitudes sounded with the lidar. We remind here that different aerosol types can be monitored
11 at the monitoring site of this study, because of its geographical location in the Central
12 Mediterranean. In fact, south eastern Italy may be affected by polluted particles from urban and
13 industrial areas of west, north, and east Europe, marine aerosols from the Mediterranean itself
14 and/or transported from the Atlantic, biomass burning particles, often produced in forest fire,
15 mainly during summer, and dust particles from the Sahara desert and the arid regions in the
16 Iberian Peninsula (Tafuro et al., 2007). Figure 3a shows the pathways estimated at 14:00 UTC
17 of the ten day analytical backtrajectories with arrival heights at 1, 2, and 3 km above the
18 ground level (a.g.l.), calculated from the Hybrid Single Particle Lagrangian Integrated
19 Trajectory Model (HYSPPLIT) (Draxler and Rolph, 2003). Advection patterns similar to the one
20 of Fig. 3a are rather frequent over southeastern Italy mainly in summer (Perrone et al., 2013).
21 The time evolution of the altitude of each backtrajectory is plotted in Fig. 3b. Figure 3a reveals
22 that the air masses reached southeastern Italy after crossing several populated regions of west,
23 north, and east Europe. More specifically, Fig. 3b shows that the 1 km-arrival-height air
24 masses travelled close to the ground level 2-3 days before their arrival time, and that the 2 km-
25 arrival-height air masses travelled close to the ground level over southeastern Spain and several
26 Eastern Europe regions. As a consequence, they were likely responsible for the lifting at high
27 altitudes of soil and local anthropogenic particles. The ground surface heating, generating
28 turbulent fluxes mainly in summer also favors the lifting of ground particles and the mixing
29 with particles located at higher altitudes. Moreover, the lack of rainy days mainly occurring in
30 summer over southern Europe enhances the natural and anthropogenic soil resuspension. In
31 fact, some of the authors found that both the aerosol load and the maximum altitude where

1 aerosols are located increase from winter to summer (De Tomasi et al., 2006). Figure 3c shows
2 that the 10-day fire map by MODIS from 20 to 29 August, 2011
3 (<https://firms.modaps.eosdis.nasa.gov/firemap/>) and we observe that the air masses overpassed
4 biomass burning areas (identified as yellow-dots in Fig. 3c) where they were likely enriched by
5 biomass burning aerosols prior to the observation. Therefore, the fine and coarse mode volume
6 concentrations (Fig. 2a) are likely due to anthropogenic pollution and biomass burning
7 particles, and resuspended soil and sea-salt particles, respectively. Dotted lines in Figs. 2b-2d
8 show the vertical profiles of $\alpha_L(\lambda_i, z)$, $LR_L(\lambda_i, z)$, and $\eta_L(\lambda_i, z)$, respectively with
9 corresponding uncertainties retrieved from LIRIC in accordance with Eqs. 2-5. The large
10 extinction coefficient values at 355 nm and the strong dependence of $\alpha_L(\lambda_i, z)$ on λ_i indicate
11 that fine mode particles were dominant, since the efficiency of scattering by small particles is
12 more pronounced at the short wavelengths (e.g. O'Neill et al., 2003; Lopatin et al., 2013). The
13 high LR values at 355 nm which span the the 79-84 sr range from the ground up to 3.9 km
14 a.g.l. (Fig. 2c, blue dotted line), also indicate that the aerosol load was affected by a significant
15 contribution of fine absorbing particles, like anthropogenic and biomass burning particles (e.g.
16 Barnaba et al., 2007; Mamouri et al., 2012 and references therein). LR values at 532 and 1064
17 nm are $\cong 54$ and 30 sr, respectively. It is worth noting that recent numerical results from
18 Lopatin et al. (2013) have revealed that the LR dependence on λ_i for fine mode absorbing
19 particles is rather close to the one revealed by Fig. 2c (dotted lines). $\eta_L(355, z)$ mean values
20 which span the 0.86-0.94 range from the ground up to 3.9 km a.g.l. furthermore show that the
21 355 nm-extinction is mainly determined by fine mode particles. η_L spans the 0.72-0.86 and the
22 0.30-0.52 range at 532 and 1064 nm, respectively (Fig. 2d), since the extinction by fine mode
23 particles decreases with the wavelength increase. Ångstrom exponent profiles with
24 corresponding uncertainties for different wavelength pairs are plotted in Figs. 4a and 4b (dotted
25 lines) and we observe that they are on average characterized by values larger than 1 from the
26 ground up to 3.9 km a.g.l. for all tested wavelength pairs, as expected when fine mode particles
27 are dominant. However, one must be aware that large fine mode particles can have the same
28 Ångstrom exponent of mixtures of coarse and small fine mode particles, as Schuster et al.
29 (2006) have clearly shown in Fig. 3 of their paper. The spectral difference $\Delta\hat{\mathring{A}}_L(z)$ can allow
30 inferring the occurrence of bimodal aerosol size distribution, according to Schuster et al.
31 (2006). Figure 4b (red dotted line) shows the vertical profile of $\Delta\hat{\mathring{A}}_L(z)$ mean values with

1 corresponding uncertainties: mean values which span the 0.02-0.32 range from the ground up
2 to 3.9 km a.g.l., indicate that the aerosol size distribution is made by two separate modes with a
3 significant coarse mode contribution (e.g. O'Neill et al., 2003; Schuster et al., 2006 and
4 references therein).

5 Aerosol extinction coefficient ($\alpha(\lambda_i, z)$) and lidar ratio ($LR(\lambda_i, z)$) profiles retrieved from the
6 constrained iterative inversion procedure by using the lidar data set used in LIRIC, are plotted
7 in Figs. 2b-2c (solid lines), respectively to investigate the LIRIC ability to retrieve vertical
8 profiles of aerosol optical parameters. Figure 2b reveals that the differences between the LIRIC
9 (dotted line) and the CII-procedure (solid lines) extinction coefficients vary with altitude and
10 wavelength and decrease with the increase of λ_i . More specifically, Fig. 2b shows that $\alpha(355$
11 $\text{nm}, z)$ values are smaller than corresponding $\alpha_L(355 \text{ nm}, z)$ values within 1-2 km a.g.l. The
12 extinction coefficient sensitivity to fine mode particles is large at 355 nm. Therefore, the
13 vertical profile of the fine-mode size distribution retrieved from LIRIC (Fig. 2a, black dotted)
14 is likely responsible for the above mentioned differences. Note that the differences between
15 $\alpha(355 \text{ nm}, z)$ and $\alpha_L(355 \text{ nm}, z)$ on average decrease with the altitude increase. Lidar ratios
16 from the CII procedure (Fig. 2c, solid lines) are in good accordance within ± 1 SD of mean
17 values with corresponding values from LIRIC (Fig. 2c, dotted lines). It is also worth noting
18 that the uncertainties associated with the CII procedure LR values are larger than the variability
19 range of corresponding LR_L values, since they vary weakly with the altitude. Note that Wagner
20 et al. (2013) also found that LR_L values were characterized by a rather weak dependence on z .
21 Hence, the differences between the LIRIC and the CII procedure aerosol extinction profiles
22 revealed by Fig. 2b are not likely due to the assumption of height-independent lidar ratios by
23 the CII procedure. Figures 4a and 4b show by solid lines the Ångström exponent profiles
24 ($\text{Å}(\lambda_1, \lambda_2, z)$) with corresponding uncertainties retrieved from the CII procedure for different
25 wavelength pairs. We remind here that Ångström exponents are good indicators of the
26 dominant aerosol size (Schuster et al., 2006 and references therein). As a consequence, the
27 $\text{Å}(\lambda_1, \lambda_2, z)$ changes with z are linked to the changes with z of the aerosol size distribution.
28 Figure 4a shows that $\text{Å}(355, 532, z)$ values (blue solid line) are smaller than the corresponding
29 $\text{Å}_L(355, 532, z)$ values (blue dotted line) up to ~ 2 km a.g.l. and take larger values at $z > 2.8$ km
30 a.g.l. By contrast, Fig. 4b reveals that $\text{Å}(355, 1064, z)$ values are in reasonable accordance with
31 the corresponding $\text{Å}_L(355, 1064, z)$ values up to ~ 3.9 km a.g.l. The Ångström sensitivity to

1 particle size which varies with the wavelength pair is responsible for these results. \AA values
2 calculated from shorter wavelength pairs (e.g. $\lambda = 355, 532 \text{ \mu m}$) are sensitive to the fine mode
3 effective radius but not the fine mode fraction, according to Schuster et al. (2006). Conversely,
4 longer wavelength pairs (e.g. $\lambda = 532, 1064 \text{ \mu m}$) are sensitive to the fine mode fraction of
5 aerosols but not the fine mode radius. In fact, Schuster et al. (2006) pointed out that it is
6 important to consider the wavelength pair used to calculate the Ångstrom exponent when
7 making qualitative assessments about the corresponding aerosol size distribution. Note that the
8 increase of $\text{\AA}(355,532, z)$ with z (Fig. 4a, solid line) is due to the increase with z of the $\alpha(355,$
9 $z)/\alpha(532, z)$ ratio (Eq. 7). Therefore, the dependence of $\text{\AA}(355,532, z)$ on z may indicate that
10 the modal radius of the fine mode particles decreases with the altitude increase. The Ångstrom
11 exponent spectral difference from LIRIC $\Delta\text{\AA}_L(z)$ (Fig. 4b, red dotted line) varies weakly with z
12 with respect to $\Delta\text{\AA}(z)$ (Fig. 4c, red solid line), which takes negative values from the ground up
13 to $\sim 2 \text{ km a.g.l.}$ and positive values at $z > 2.7 \text{ km a.g.l.}$ More specifically, Fig. 4b (solid red
14 line) shows that $\Delta\text{\AA}(z)$ on average increases with z . The increase with z of the fine mode
15 particle contribution is likely responsible for this result, in accordance with Eq. 8. In
16 conclusion, the comparison of Ångstrom exponent and spectral difference profiles from LIRIC
17 and the CII-procedure has revealed some marked differences which have likely been
18 determined by the LIRIC assumption that aerosol modal radii are invariant over the altitude.
19 Calculated $\Delta\text{\AA}_L(z)$ versus $\text{\AA}_L(355,1064, z)$ values within 1-3.9 km a.g.l. are plotted on the
20 graphical framework of Fig. 5 (open triangles) to investigate to what extent, the estimates of
21 the fine mode radius ($R_{f,GF}$) and of the fine mode fraction (η_{GF}) from the graphical framework
22 (Section 2.4) are in accordance with corresponding LIRIC results. The triangle size in Fig. 5
23 accounts for the $\Delta\text{\AA}_L(z)$ and $\text{\AA}_L(355,1064, z)$ uncertainties. Different colors are used to
24 represent $\Delta\text{\AA}_L(z)$ vs $\text{\AA}_L(355,1064, z)$ values referring to different z , as indicated by the color
25 bar on the right of Fig. 5. Data at $z \leq 1 \text{ km}$ have not been plotted since they are likely affected
26 by the lidar field of view: the lidar system is estimated to achieve full overlap at $z \geq 1 \text{ km a.g.l.}$
27 (Section 2.2). The graphical framework calculated for $n = 1.455$ and $k = 0.0047$ at 532 nm
28 (Mixed aerosol framework) is shown in Fig. 5. These refractive index values are considered
29 representative of aerosol loads affected by mixed aerosol types, in accordance with the
30 discussion reported in Perrone et al. (2014). It is interesting to observe: 1) that the $\Delta\text{\AA}_L(z)$ vs
31 $\text{\AA}_L(355,1064, z)$ values are on the framework area delimited by η_{GF} values spanning the ~ 70 -

1 80% range, in good accordance with the $\eta_L(532, z)$ values of Fig 2d (green dotted line) and 2
 2 that all data points are located on the $R_{f,GF} \cong 0.09 \mu\text{m}$ curve, in satisfactory accordance with the
 3 columnar averaged aerosol fine modal radius retrieved from AERONET which is $R_{f,A} = 0.085$
 4 μm . The fine modal radius is calculated from the value of the AERONET fine volume median
 5 radius $R_{Vf,A}(\mu\text{m})$ by the following relationship (Seinfeld and Pandis, 1998):

$$\ln R_{f,A} = \ln R_{Vf,A} - 3 \ln^2 \sigma_g \quad (9)$$

6
 7
 8
 9 where σ_g represents the geometric standard deviations for fine mode particle, that is an
 10 AERONET aerosol product. Note that these results reveal the feasibility of the graphical
 11 framework to provide a good estimate of the fine mode fraction and the fine modal radius
 12 retrieved from LIRIC. Full dots and error bars in Fig. 5 show for comparison $\Delta\hat{A}(z)$ vs
 13 $\hat{A}(355,1064, z)$ mean values with corresponding standard deviations. It is interesting to
 14 observe that the $\Delta\hat{A}(z)$ vs $\hat{A}(355,1064, z)$ mean values are on the graphical framework area
 15 delimited by η_{GF} values spanning the 70%-99% range, in satisfactory accordance with LIRIC
 16 results, and $R_{f,GF}$ values 2) that the particle fine modal radius varies with z spanning the ~ 0.02 -
 17 $0.17 \mu\text{m}$ range, in contrast to LIRIC results (triangle). Note that the ~~CH-procedure does not~~
 18 ~~make any constrain on the dependence on altitude of the particle size. The~~ selection of a
 19 height-independent LR to match the AOT represents the main source of uncertainties of the
 20 CII-procedure, according to Perrone et al. (2014). Therefore, if we assume that the graphical
 21 framework can provide a reliable estimate of the fine particle modal radius, the $\Delta\hat{A}(z)$ versus
 22 $\hat{A}(355,1064, z)$ scatter plot (Fig. 5, full dots) shows that the fine particle modal radius
 23 decreases with the altitude increase. Figure 5 also shows that the value of $R_{f,GF} \cong 0.09 \mu\text{m}$
 24 retrieved from LIRIC locates on the middle of variability range of the fine particle modal radii
 25 retrieved from the $\Delta\hat{A}(z)$ versus $\hat{A}(355,1064, z)$ plot. Backtrajectory pathways (Figs. 3a-3b)
 26 and the MODIS fire map (Fig. 3c), which have indicated that aerosol from different sources
 27 have contributed to the aerosol load monitored by the lidar on August 29, 2011, can support the
 28 dependence on z of the fine modal radius revealed by Fig. 5 (full dots). The gravitational
 29 settling of large fine mode particles has likely contributed to the decrease of the fine modal
 30 radius with the altitude increase revealed by Fig. 5 (full dots). Note that the lack of rainy days
 31 occurring on summer over the central Mediterranean favors the aging of aerosol and likely the

1 gravitational settling of large fine mode particles. Moreover, the large solar flux on summer
2 time favors the formation of new anthropogenic particles by photochemical reactions (Seinfeld
3 and Pandis, 1998). Note that the fine modal radius estimates retrieved from the $\Delta\hat{A}(z)$ versus
4 $\hat{A}(355, 1064, z)$ scatter plot (Fig. 5, full dots) can allow understanding the differences between
5 $\alpha_L(355 \text{ nm}, z)$ and $\alpha(355 \text{ nm}, z)$ revealed by Fig. 2b (blue lines) within 1-2 km a.g.l. In fact,
6 the large values of the fine modal radius within 1-2 km a.g.l. (Fig. 5, full dots) have likely been
7 responsible for the smaller $\alpha(355 \text{ nm}, z)$ values with respect to the $\alpha_L(355 \text{ nm})$ values. In
8 conclusion, the above comments may lead to infer that the search of height-independent
9 aerosol fine and coarse modal radii can represent the main source of uncertainties of the
10 LIRIC aerosol products and hence, the main limit of the LIRIC method. Therefore, the
11 uncertainties of the LIRIC aerosol products may be significant mainly when aerosols from
12 different sources and hence, characterized by different size distributions, affect the whole
13 aerosol load, as commonly occurs over the Central Mediterranean (e.g. Perrone et al., 2014).

14

15 **3.2 Case study: September 12, 2011**

16

17 Figure 6a shows the vertical profiles of the mean fine $C_{f,a}(\lambda_i, z)$ and coarse $C_{c,a}(\lambda_i, z)$ particle
18 volume concentration with corresponding standard deviations (error bars), retrieved from
19 LIRIC by combining lidar measurements performed on September 12, 2011 from 14:06 to
20 14:36 UTC and AERONET inversion products, retrieved from sun/sky photometer
21 measurements (Lecce University) performed at 14.21 UTC. Fine and coarse particle volume
22 concentrations vary similarly with the altitude but, fine particle volume concentrations are
23 nearly 1.5 larger than coarse particle volume concentrations. Note that previous analyses of the
24 Lecce University-AERONET inversion products have revealed that the columnar aerosol
25 volume size distribution is on average bimodal and that fine mode particles are dominant
26 during all year (Tafuro et al., 2007; Bergamo et al., 2008). The bimodal structure of the size
27 distribution spectrum indicates that along with fine mode particles, which are mainly of
28 anthropogenic origin, coarse mode particles as those of natural (marine and crustal) origin, also
29 contribute to the aerosol load during all year. Dotted lines in Figs. 6b-6d show the vertical
30 profiles of $\alpha_L(\lambda_i, z)$, $LR_L(\lambda_i, z)$, and $\eta_L(\lambda_i, z)$, respectively with corresponding uncertainties
31 calculated in accordance with the methodology outlined in Section 2.1. The extinction

1 coefficient profiles indicate that a vertically homogeneous layering of aerosol particles was
2 detected from the lidar from the ground up to ~ 3 km a.g.l. Lidar ratio values that vary rather
3 weakly with z , are equal to about 25, 60 and 75 sr at 1064, 532, and 355 nm, respectively.
4 These values have likely been determined by the significant contribution of fine absorbing
5 particles (Lopatin et al., 2013). $\eta_L(355, z)$, $\eta_L(532, z)$, and $\eta_L(1064, z)$ mean values span the
6 0.95-0.99, 0.90-0.99, and 0.60-0.95 range, respectively from the ground up to ~ 4.2 km a.g.l.
7 The Ångström exponent vertical profiles for different wavelength pairs are plotted in Fig. 7a-b
8 (dotted lines). They take values > 1.5 for all tested wavelength pairs up to ~ 3 km a.g.l. as it
9 occurs when fine mode particles are dominant. The pathways of the seven day HYSPLIT
10 backtrajectories with arrival heights at 0.5, 1.5, and 2.5 km a.g.l. (Figs. 8a-8b) at 14:00 UTC of
11 September 12, 2011, can support the aerosol properties revealed by Figs. 6-7. Figure 8a shows
12 that the 0.5 km air masses crossed the Tyrrhenian Sea at quite low altitudes before reaching
13 southern Italy and as a consequence they have likely been responsible for the advection of sea-
14 salt particles. By contrast, the 1.5 and 2.5 km air masses which have their origin over the
15 Atlantic Sea at high altitudes are characterized by a similar pathway and reached Southeastern
16 Italy after crossing Central Europe and the eastern coast of the Adriatic Sea. Therefore, they
17 have mainly been responsible for the advection of anthropogenic pollution and sea-salt
18 particles lifted up to ~ 3 km a.g.l. Solid lines in Figs. 6b and 6c show the aerosol extinction
19 coefficient and lidar ratio profiles retrieved from the constrained iterative inversion procedure.
20 The differences between the CII-procedure (solid lines) and the LIRIC (dotted line) extinction
21 coefficients vary with altitude and wavelength and decrease with the increase of λ_i . More
22 specifically, they are within ± 1 SD of mean values at 1064 nm, while $\alpha(355 \text{ nm}, z)$ values are \sim
23 1.1 times larger than the corresponding $\alpha_L(355 \text{ nm}, z)$ values from the ground up to ~ 1.9 km
24 a.g.l. Lidar ratios (Fig. 6c) from the CII-procedure are in accordance within ± 1 SD of mean
25 values with corresponding values from LIRIC, which show a rather weak dependence on z , as
26 mentioned. Ångström exponent profiles from the CII procedure also are in reasonable
27 accordance with the corresponding profiles from LIRIC, within ± 1 SD of mean values and up
28 to ~ 3 km a.g.l. Both the LIRIC and the CII aerosol parameters indicates that the aerosol
29 microphysical properties were characterized by a weak dependence on altitude on the
30 afternoon of September 12. This result may be due to the fact that the 1.5 and 2.5 km air
31 masses have followed the same pathway before reaching southern Italy and as a consequence,

1 they have likely been responsible for the advection of particles with similar optical and
2 microphysical properties within ~1-3 km a.g.l. Open triangles in Fig. 9 show $\Delta\hat{A}_L(z)$ versus
3 $\hat{A}_L(355,1064, z)$ within 1-3 km a.g.l. $\Delta\hat{A}_L(z)$ vs $\hat{A}_L(355,1064, z)$ values are on the framework
4 area delimited by η_{GF} values spanning the ~85-95% range, in reasonable accordance with the
5 $\eta_L(532, z)$ values of Fig 2d (green dotted line) and are located on the $R_{f,GF} \cong 0.09 \mu\text{m}$ curve.
6 This value is in satisfactory accordance with the columnar averaged aerosol fine modal radius
7 retrieved from AERONET which is $R_{f,A} = 0.082 \mu\text{m}$. Note that the $\Delta\hat{A}_L(z)$ vs $\hat{A}_L(355,1064, z)$
8 plot shows ones more the feasibility of the graphical framework to provide a good estimate of
9 the fine mode fraction and the fine modal radius retrieved from LIRIC. Full dots in Fig. 9
10 show the scatterplot of $\Delta\hat{A}(z)$ versus $\hat{A}(355,1064, z)$ with corresponding uncertainties (error
11 bars) within 1-3 km a.g.l. Different colors are used to represent values referring to different z ,
12 as indicated by the color bar on the right of Fig. 9. $\Delta\hat{A}(z)$ vs $\hat{A}(355,1064, z)$ mean values are on
13 the graphical framework area delimited by η_{GF} and $R_{f,GF}$ values spanning the 90%-99% and
14 the 0.08-0.10 μm range, in satisfactory accordance with the corresponding parameters from
15 LIRIC. Hence, Fig. 9 reveals that the aerosol products from LIRIC are in better accordance
16 with the corresponding ones from the CII procedure, when the particle fine modal radius varies
17 weakly with the altitude.

18

19 **3.3 Case study: August 6, 2012**

20

21 The last case study deals with lidar measurements performed on August 6, 2012. Aerosol
22 affected by Sahara dust particles were monitored on August 6, as shown in the following.
23 Figure 10 (black line) shows the vertical profile of the linear particle depolarization-ratio
24 ($\delta_p(z)$) with corresponding uncertainties (Perrone et al., 2014), calculated from lidar
25 measurements at 355 nm performed on August 6, 2012 from 14:57 to 15:21 UTC. The $\delta_p(z)$
26 mean values that are $\cong 20\%$ within 2-5 km a.g.l. show the altitude range affected by non
27 spherical particles. Then, analytical backtrajectories and the BSC-DREAM model indicate that
28 the $\delta_p(z)$ values were determined by the advection of Sahara dust particles. Figure 11 shows the
29 pathways estimated at 15:00 UTC of August, 6, 2012, of the 10 day HYSPLIT backtrajectories
30 with arrival heights at 1, 2.5, and 4.5 km a.g.l. We observe that the 2.5 km air masses crossed

1 northern Morocco at very low altitudes (Fig. 11b) and that the 4.5 km air masses crossed
2 central Algeria and Morocco at very low altitudes (Fig. 11b) before reaching southeastern Italy.
3 So, they have likely been responsible for the advection of Sahara dust particles lifted from the
4 ground up ~ 5 km a.g.l. The 1 km air masses have their origin over the Atlantic and travelled at
5 high altitudes before reaching southern Italy. The advection of Sahara dust particles over
6 southern Italy occurred from midday of August 4 up to the night of August 9, in accordance
7 with the BSC-DREAM simulations ([http://www.bsc.es/earth-sciences/mineral-dust-forecast-](http://www.bsc.es/earth-sciences/mineral-dust-forecast-system/bsc-dream8b-forecast/north-africa-europe-and-middle-ea-0)
8 [system/bsc-dream8b-forecast/north-africa-europe-and-middle-ea-0](http://www.bsc.es/earth-sciences/mineral-dust-forecast-system/bsc-dream8b-forecast/north-africa-europe-and-middle-ea-0)). The red line in Fig. 10
9 shows the vertical profile of the dust particle concentration simulated from the BSC-DREAM
10 for the monitoring site of this study, at 12:00 UTC of August 6. Figure 10 (red line) reveals the
11 existence of a dust layer extending from the ground up to ~ 5 km a.g.l., with mass
12 concentrations larger than $70 \mu\text{g}/\text{m}^3$ at ~ 2 km a.g.l. Note that the dust concentration profile of
13 Fig. 10 (red line) supports the $\delta_p(z)$ profile (Fig. 10, black line) retrieved from lidar
14 measurements. It is also worth noting that during the Saharan Mineral Dust Experiment
15 campaigns, dust depolarization ratios were around 0.23-0.25 at 355 nm (Wagner et al., 2013),
16 in satisfactory accordance with the results of this study (Fig. 10, black line). Figure 12a shows
17 the mean fine $C_{f,a}(\lambda_i, z)$ and coarse $C_{c,a}(\lambda_i, z)$ particle volume concentration profiles with
18 corresponding ± 1 SD of mean values (error bars). They have been retrieved from LIRIC by
19 combining lidar measurements performed on August 6, 2012 from 14:57 to 15:21 UTC and
20 AERONET inversion products from sun/sky photometer measurements (Lecce University)
21 performed at 15.13 UTC. Coarse particle volume concentrations are dominant up to ~ 5 km
22 a.g.l. in satisfactory accordance with particle depolarization ratio measurements, dust particle
23 concentration from the BSC-DREAM (Fig. 10) and backtrajectory pathways (Fig. 11). Dotted
24 lines in Fig. 12b show the LIRIC extinction coefficient vertical profiles at 355, 532 and 1064
25 nm with the corresponding ± 1 SD of mean values (error bars). A vertically inhomogeneous
26 layering of aerosol particles was detected by the lidar within 1-7 km a.g.l. The detected aerosol
27 layering may be supported by the vertical structure of the potential temperature (θ) and relative
28 humidity (RH) profiles (Fig. 13), which have been retrieved from radiosonde measurements
29 performed at the meteorological station of Brindisi (<http://esrl.noaa.gov/raobs/>) on 6 August at
30 11:00 UTC. Figure 13 (full dots) reveals that the potential temperature increases with altitude
31 and shows a temperature inversion at about 0.5, 1.8, and 5 km a.g.l. The RH profile (Fig. 13

1 open dots) is also quite dependent on altitude. RH takes rather small values (10-20%) within 1-
 2 3.2 km a.g.l and then increases with z reaching the value of 60% at ~ 4.8 km a.g.l. These results
 3 indicate that rather dry particles were located within 1-3.2 km a.g.l. Dotted lines in Figs. 12c
 4 and 12d show the vertical profiles of $LR_L(\lambda_i, z)$ and $\eta_L(\lambda_i, z)$, respectively with corresponding
 5 ± 1 SD of mean values (error bars). Lidar ratio values span the 84-71 sr, 61-56 sr, and 51-47 sr
 6 range at 355, 532, and 1064 nm, respectively and decrease slowly with z . The fine mode
 7 fractions increase with z spanning the 0.10-0.88, 0.06-0.74, and 0.02-0.40 range at 355, 532,
 8 and 1064 nm, respectively, from the ground up to ~ 5.4 km a.g.l. Solid lines in Figs. 12b and
 9 12c show the aerosol extinction coefficient and lidar ratio profiles, respectively retrieved from
 10 the constrained iterative inversion procedure. The differences between the CII-procedure (solid
 11 lines) and the LIRIC (dotted line) extinction coefficients vary significantly both with the
 12 altitude and the lidar wavelength (Fig. 12 b). Mean lidar ratios from the CII-procedure that are
 13 equal to 64 ± 10 , 56 ± 8 and 47 ± 18 sr at 355, 532, and 1064 nm, respectively, are typical of
 14 Sahara dust particles, in accordance with previous studies (e.g. Wagner et al., 2013; Perrone et
 15 al., 2014 and references therein). The lidar ratio values from the CII procedure at 1064 nm and
 16 532 nm are in good accordance within ± 1 SD of mean values, with the corresponding values
 17 from LIRIC. By contrast, the $LR_L(355, z)$ values are larger than the corresponding $LR(355, z)$
 18 values from the ground up to ~ 5.4 km a.g.l. Dotted and solid lines in Fig. 14a-b show the
 19 Ångstrom exponents for different wavelength pairs retrieved from LIRIC and the CII-
 20 procedure extinction coefficient, respectively up to 5.4 km a.g.l. The differences between \hat{A}_L
 21 and corresponding \hat{A} values vary significantly with altitude and wavelength pairs. In fact,
 22 $\hat{A}_L(532, 1064, z)$ and corresponding $\hat{A}(532, 1064, z)$ values are in satisfactory accordance
 23 within ± 1 SD from 1.5 up 5.4 km a.g.l. By contrast, the $\hat{A}(355, 532, z)$ values are smaller than
 24 the corresponding $\hat{A}_L(355, 532, z)$ values within 2.5-4.5 km a.g.l. Red solid and dotted lines in
 25 Fig. 14b show the vertical profile of the spectral curvature from the CII-procedure and LIRIC,
 26 respectively. $\Delta\hat{A}(z)$ values vary from about -1 up to 1 within 1.0-5.4 km a.g.l. By contrast, the
 27 $\Delta\hat{A}_L(z)$ values are close to zero within the same altitude range. Open triangles in Fig. 15 show
 28 $\Delta\hat{A}_L(z)$ versus $\hat{A}_L(355, 1064, z)$ from 1 up to 5.4 km a.g.l. Different colors represent $\Delta\hat{A}_L$ vs \hat{A}_L
 29 values referring to different z , as indicated by the color bar on the right of Fig. 15. The triangle
 30 size accounts for the $\Delta\hat{A}_L(z)$ and $\hat{A}_L(355, 1064, z)$ uncertainties. The blue solid and dashed lines
 31 of Fig. 15 represent the Dust rev. coarse graphical framework, since it is considered best suited

1 for aerosol loads heavily affected by desert dust particles, in accordance with the discussion of
 2 Section 2.4. $\Delta\hat{A}_L$ vs \hat{A}_L mean values are on the graphical framework area delimited by η_{GF}
 3 values varying up to ~70% in good accordance with the $\eta_L(532 \text{ nm}, z)$ variability range (Fig.
 4 12d), and are mainly located on the $R_{f,GF} \cong 0.1 \text{ }\mu\text{m}$ solid line, since the LIRIC method does not
 5 allow to the fine modal radius to change with z . Note that the columnar averaged aerosol fine
 6 modal radius from AERONET is $R_{f,A} = 0.041 \text{ }\mu\text{m}$. The rather low $R_{f,A}$ value retrieved from
 7 AERONET is likely due to the fact that the Dubovik inversion procedure overestimates the
 8 fine mode fraction for dust-dominated aerosol conditions, according to Kleidman et al. (2005).
 9 We believe that the $\Delta\hat{A}_L$ vs \hat{A}_L plot shows once again that the graphical framework can provide
 10 a reliable estimate of the particle fine mode fraction and of the fine particle modal radius
 11 retrieved from LIRIC. Full dots and error bars in Fig. 15 show $\Delta\hat{A}(z)$ versus $\hat{A}(355, 1064, z)$
 12 with corresponding uncertainties within 1-5.4 km a.g.l. $\Delta\hat{A}$ vs \hat{A} mean values are on the
 13 graphical framework area delimited by η_{GF} values varying up to ~70% (in good accordance
 14 with LIRIC results) and $R_{f,GF}$ values spanning the 0.02-0.3 μm range. The main differences
 15 between the $\Delta\hat{A}_L(z)$ vs $\hat{A}_L(355, 1064, z)$ and the $\Delta\hat{A}(z)$ vs $\hat{A}(355, 1064, z)$ plot are due to the
 16 fact that the $\Delta\hat{A}(z)$ vs $\hat{A}(355, 1064, z)$ data points show that the fine modal radius vary with the
 17 altitude range. This result can be supported by the backtrajectory pathways of Fig. 11 which
 18 vary with the arrival height. It is well known that the optical and microphysical properties of
 19 advected particles are quite dependent on both the source regions and the pathways they have
 20 followed before reaching the monitoring site. The $\Delta\hat{A}(z)$ vs $\hat{A}(355, 1064, z)$ plot indicates that
 21 the data points within ~1-2.2 km a.g.l. are on the graphical framework area delimited by $R_{f,GF}$
 22 values spanning the 0.02-0.15 μm range. By contrast, the $\Delta\hat{A}(z)$ vs $\hat{A}(355, 1064, z)$ mean
 23 values within ~2.2-4.8 km a.g.l. are on the graphical framework area delimited by $R_{f,GF}$ values
 24 spanning the 0.1-0.3 μm range. The depolarization lidar measurements, the BSC-DREAM dust
 25 concentration profile, and backtrajectory pathways support last results, since they indicate that
 26 the contribution of Sahara dust particles is greater within 2-5 km a.g.l. It is also worth noting
 27 that the $R_{f,GF} \cong 0.1 \text{ }\mu\text{m}$ value retrieved from the $\Delta\hat{A}_L(z)$ vs $\hat{A}_L(355, 1064, z)$ plot is located
 28 within the $R_{f,GF}$ variability range ($\cong 0.02\text{-}0.3 \text{ }\mu\text{m}$) retrieved from the $\Delta\hat{A}(z)$ vs $\hat{A}(355, 1064, z)$
 29 plot. Finally, it is worth mentioning that the dependence on z of the fine modal radius estimates
 30 from the $\Delta\hat{A}(z)$ vs $\hat{A}(355, 1064, z)$ plot, can allow understanding the differences between $\alpha_L(\lambda_i,$

1 z) and $\alpha(\lambda_i, z)$ revealed by Fig. 12b. In fact, the larger values of the fine modal radius estimates
2 from the $\Delta\text{\AA}(z)$ vs $\text{\AA}(355,1064, z)$ plot are likely responsible for the smaller values of $\alpha(\lambda_i, z)$
3 within ~ 2.5 - 4.8 km a.g.l. (Fig. 12b), with respect to the corresponding $\alpha_L(\lambda_i, z)$ values. Hence,
4 the analysis of this last case study has once again indicated that the differences between the
5 aerosol products from LIRIC and the CII procedure can be quite large when the fine modal
6 radius and hence the aerosol size distribution vary with the altitude.

7

8

9 **4 Summary and conclusion**

10

11 The potential of LIRIC to retrieve the vertical profiles of fine- and coarse-mode particle
12 volume concentrations by combining AERONET sun/sky photometer aerosol products and 3-
13 wavelength elastic lidar signals, has been investigated. An aerosol classification framework,
14 which allows estimating the dependence on altitude of the aerosol fine modal radius and of the
15 fine mode fraction from the Ångstrom exponent spectral difference ($\Delta\text{\AA}$) versus the 355-1064
16 nm-Ångstrom exponent plot, has been used to investigate the potential of LIRIC to retrieve the
17 vertical profiles of fine- and coarse-mode particle volume concentrations. The LIRIC ability to
18 retrieve the vertical profiles of aerosol extinction coefficients ($\alpha_L(\lambda_i, z)$), lidar ratios ($\text{LR}_L(\lambda_i,$
19 $z)$), Ångstrom exponents ($\text{\AA}_L(\lambda_1, \lambda_2, z)$) for different wavelength pairs, and of the spectral
20 difference ($\Delta\text{\AA}_L$), has been investigated by comparing LIRIC results with the corresponding
21 ones from a constrained iterative inversion procedure. The CII-procedure that is based on the
22 assumption of a lidar ratio constant over the altitude, allows retrieving aerosol extinction
23 coefficient $\alpha(\lambda_i, z)$ and lidar ratio $\text{LR}(\lambda_i, z)$ profiles from 3-wavelength lidar measurements by
24 using as boundary conditions: (1) the AOT of a selected altitude range and (2), the total
25 backscatter coefficient β_T (due to molecules (β_M) and aerosol (β)) at a far-end reference height
26 z_f . It is also assumed (3) that the aerosol optical and microphysical properties are constant from
27 the ground up to the height z_0 where the lidar system is estimated to achieve full overlap and
28 (4) that the AOTs at the lidar wavelengths are retrieved from co-located in space and time
29 AERONET measurements. Note that constrains (1) - (4) are common to LIRIC. In addition,
30 LIRIC that is an algorithm for solving inverse problems, searches the concentration profiles
31 that best match the multi wavelength lidar measurements, by also requiring that the integral of

1 ~~the retrieved concentrations for particle lidar profiles that best~~ matches the AERONET-derived
2 column volume concentrations, to retrieve the vertical profiles of fine $C_f(\lambda_i, z)$ and coarse
3 $C_c(\lambda_i, z)$ particle volume concentrations.

4 Three case studies with different aerosol load scenarios have been analyzed to investigate the
5 LIRIC retrieval ability. One case study deals with aerosol measurements affected by
6 anthropogenic, biomass-burning, and soil particles. The second case study deals with
7 anthropogenic pollution likely affected by marine aerosol and the last one deals with aerosols
8 significantly affected by Sahara dust. The comparison of the LIRIC extinction coefficient
9 profiles with the corresponding profiles from the CII-procedure has revealed for all study
10 cases, that the differences between $\alpha_L(\lambda_i, z)$ and $\alpha(\lambda_i, z)$ vary with altitude and wavelength and
11 decrease with the increase of λ_i . The comparison of Ångstrom exponent profiles has revealed
12 that the differences between $\mathring{A}_L(\lambda_1, \lambda_2, z)$ and $\mathring{A}(\lambda_1, \lambda_2, z)$ vary with z and the wavelength pair.
13 Ångstrom exponents are good indicators of the dominant aerosol size; however, their
14 sensitivity to the aerosol size varies with the wavelength pair. Hence, the Ångstrom exponent
15 inter comparison has clearly indicated that the differences between $\mathring{A}_L(\lambda_1, \lambda_2, z)$ and $\mathring{A}(\lambda_1, \lambda_2, z)$
16 are mainly linked to the changes with z of the aerosol size distribution retrieved from LIRIC.
17 The plot on the aerosol classification framework of the Ångstrom exponent spectral difference
18 versus the 355-1064 nm-Ångstrom exponent has revealed for all case studies that the data
19 retrieved from LIRIC and the CII-procedure are on average on a framework area characterized
20 by rather similar fine mode fraction values. However, LIRIC data are on average located on a
21 curve with nearly constant fine modal radius while, the CII- procedure data points are spread
22 on a framework region revealing that the fine modal radius is dependent on the altitude a.g.l.
23 The results from the aerosol classification framework have also allowed inferring that the
24 deviations between the LIRIC aerosol parameters and the corresponding CII-procedure aerosol
25 parameters are mainly due to the fact that LIRIC does not allow to the modal radius of fine
26 mode particles to vary with the altitude. In fact, the analysis of the three case studies has
27 revealed that the differences between the aerosol products from LIRIC and the CII-procedure
28 are quite large when aerosol from different sources and/or from different advection routes are
29 located at the altitudes sounded by the lidar. To this end, it is worth noting that the analysis of
30 the 12 September, 2011 lidar measurements has revealed that the aerosol properties were
31 weakly dependent on z within 1-3 km a.g.l., in accordance with the backtrajectory pathways.

1 Then, we have found that the differences between the LIRIC aerosol products and the
2 corresponding ones resulting from the CII-procedure were on average smaller than the ones
3 resulting from the other two study cases. However, one must be aware that several studies have
4 revealed that aerosol from different sources and/or from different advection routes are
5 commonly advected at different altitudes a.g.l. over the Central Mediterranean. So, the
6 uncertainties of the LIRIC aerosol products may be large when the LIRIC method is applied to
7 lidar measurements performed over the Mediterranean basin. In conclusion, the paper has
8 contributed to the characterization of numerical procedures that allow determining the
9 dependence on altitude of aerosol properties from multi wavelength elastic lidar signals. In
10 particular, the paper has furthermore revealed the ability of the aerosol classification
11 framework to estimate the dependence on altitude of the aerosol fine modal radius and of the
12 fine mode fraction by the Ångström exponent spectral difference versus the 355-1064 nm-
13 Ångström exponent plot. We believe that the LIRIC retrieval ability could be improved by
14 taking into account the results on the changes with z of the fine modal radius, resulting from
15 the aerosol classification framework by using the Ångström exponent profiles retrieved from
16 the CII-procedure. Work is on progress in this direction.

17

18 **Acknowledgements**

19

20 Work supported by the European Community through the ACTRIS Research Infrastructure
21 Action under the 7th Framework Programme under ACTRIS Grant Agreement n° 262254.
22 The authors gratefully acknowledge G. P. Gobbi for providing the Å-ΔÅ aerosol
23 classification frameworks. The authors would also like to acknowledge the NASA/Goddard
24 Space Flight Center and the Barcelona Super-Computing Centre for their contribution with
25 satellite images, and DREAM dust profiles, respectively. The authors gratefully acknowledge
26 the NOAA Air Resources Laboratory (ARL) for the provision of the HYSPLIT
27 backtrajectories used in this publication.

28

1 **References**

- 2
3 Ansmann, A., Seifert, P., Tesche, M., and Wandinger, U.: Profiling of fine and coarse
4 particle mass: case studies of Saharan dust and Eyjafjallajökull/Grimsvötn volcanic plumes,
5 *Atmos. Chem. Phys.*, 12, 9399–9415, doi:10.5194/acp-12-9399-2012, 2012.
- 6 Barnaba, F., Tafuro, A. M., De Tomasi, F., and Perrone, M.R.: Observed and simulated
7 vertically resolved optical properties of continental aerosols over southeastern Italy: A closure
8 study, *J. Geophys. Res.*, 112, D10203, doi:10.1029/2006JD007926, 2007.
- 9 Bergamo A., Tafuro A. M., Kinne, S., De Tomasi, F., Perrone, M. R.: Monthly-averaged
10 anthropogenic aerosol direct radiative forcing over the Mediterranean from AERONET derived
11 aerosol properties. *Atmos. Chem. Phys.*, 8, 6995-7014, 2008.
- 12 Chaikovsky, A., Dubovik, O., Goloub, P., Tanre, D., Pappalardo, G., Wandinger, U.,
13 Chaikovskaya, L., Denisov, S., Grudo, Y., Lopatsin, A., Karol, J., Lapyonok, T., Korol, M.,
14 Osipenko, F., Savitski, D., Slesar, A., Apituley, A., Alados Arboledas, L., Biniotoglou, I.,
15 Kokkalis, P., Granados Munoz, M. J., Papayannis, A., Perrone, M. R., Pietruczuk, A., Pisani,
16 G., Rocadenbosch, F., Sicard M., De Tomasi, F., Wagner, J., Wang, X.: Algorithm and
17 software for the retrieval of vertical aerosol properties using combined lidar/radiometer data:
18 dissemination in EARLINET, Reviewed & Revised Papers of the 26th International Laser
19 Radar Conference, 25-29 June, Porto Heli, Greece, Paper SO3-09, 2012.
- 20 De Tomasi, F., and Perrone, M.R.: Lidar measurements of tropospheric water vapor and
21 aerosol profiles over southeastern Italy, *J. Geophys. Res.*, 108, 4286 – 4297, 2003.
- 22 De Tomasi, F., Tafuro, A.M., and Perrone, M.R.: Height and seasonal dependence of
23 aerosol optical properties over southeast Italy, *J. Geophys. Res.*, 111, D10203,
24 doi:10.1029/2005JD006779 2006.
- 25 Draxler, R.R. and Rolph, G.D.: HYSPLIT (HYbrid Single-Particle Lagrangian Integrated
26 Trajectory) model, <http://www.arl.noaa.gov/ready/hysplit4.html>, (last access May 2014)
27 NOAA Air Resources Laboratory, Silver Spring, MD, 2003.
- 28 Dubovik, O. and King, M.: A flexible inversion algorithm for retrieval of aerosol optical
29 properties from Sun and sky radiance measurements, *J. Geophys. Res.*, 105, 20673–20696,
30 doi:10.1029/2000JD900282, 2000.

1 Dubovik, O.: Optimization of numerical inversion in photopolarimetric remote sensing, in:
2 Photopolarimetry in Remote Sensing, edited by: Videen, G., Yatskiv, Y., and Mishchenko, M.,
3 65–106, Kluwer Academic Publishers, Dordrecht, The Netherlands, 2004.

4 Dubovik, O., Sinyuk, A., Lapyonok, T., Holben, B. N., Mishchenko, M., Yang, P., Eck, T.
5 F., Volten, H., Munoz, O., Veihelmann, B., van der Zande, W. J., Leon, J.-F., Sorokin, M., and
6 Slutsker, I.: Application of spheroid models to account for aerosol particle nonsphericity in
7 remote sensing of desert dust, *J. Geophys. Res.*, 111, D11208, doi:10.1029/2005JD006619,
8 2006.

9 Gobbi, G. P., Kaufman, Y. J., Koren, I., and Eck, T. F.: Classification of aerosol properties
10 derived from AERONET direct sun data, *Atmos. Chem. Phys.*, 7, 453–458, 2007.

11 Holben, B.: AERONET-A federated instrument network and data archive for aerosol
12 characterization, *Remote Sens. Environ.*, 66, 1–16, 1998.

13 Kleidman, R.G., O'Neill, N.T., Remer, L.A., Kaufman, Y.J., Eck, T.F., Tanrè, D.,
14 Dubovik, O., Holben, B.N.: Comparison of Moderate Resolution Imaging
15 Spectroradiometer (MODIS) and Aerosol Robotic Network (AERONET) remote-sensing
16 retrievals of aerosol fine mode fraction over ocean. *J. Geophys. Res.* 110, D22205, 2005,
17 doi: 10.1029/2005JD005760.

18 Lopatin, A., Dubovik, O., Chaikovsky, A., Goloub, Ph., Lapyonok, T., Tanre, D., and
19 Litvinov, P.: Enhancement of aerosol characterization using synergy of lidar and sun –
20 photometer coincident observations: the GARRLiC algorithm, *Atmos. Meas. Tech.*, 6, 2065–
21 2088, doi:10.5194/amt-6-2065-2013.

22 Mamouri, R. E., Papayannis, A., Amiridis, V., Muller, D., Kokkalis, P., Rapsomanikis, S.,
23 Karageorgos, E. T., Tsaknakis, G., Nenes, A., Kazadzis, S., and Remoundaki, E.: Multi-
24 wavelength Raman lidar, sun photometric and aircraft measurements in combination with
25 inversion models for the estimation of the aerosol optical and physico-chemical properties over
26 Athens, Greece. *Atmos. Meas. Tech.*, 5, 1793–1808, 2012. doi:10.5194/amt-5-1793-2012.

27 Matthias, V., Balis, D., Bosenberg, J., Eixmann, R., Iarlori, M., Komguem, L., Mattis, I.,
28 Papayannis, A., Pappalardo, G., Perrone, M. R., and Wang, X.: Vertical aerosol distribution
29 over Europe: Statistical analysis of Raman lidar data from 10 European Aerosol Research
30 Lidar Network (EARLINET) stations, *J. Geophys. Res.*, 109, D18201,
31 doi:10.1029/2004JD004638, 2004.

1 Müller, D., Veselovskii, I., Kolgotin, A., Tesche, M., Ansmann, A., and Dubovik,
2 O.: Vertical profiles of pure dust and mixed smoke–dust plumes inferred from inversion of
3 multiwavelength Raman/polarization lidar data and comparison to AERONET retrievals
4 and in situ observations, *Appl. Optics*, 52, 3178-3202, 2013.

5 O’Neill, N. T., Eck, T. F., Smirnov, A., Holben, B. N., and Thulasiraman, S.: Spectral
6 discrimination of coarse and fine mode optical depth, *J. Geophys. Res.*, 108, 4559,
7 doi:10.1029/2002JD002975, 2003.

8 Perrone, M. R., Tafuro, A. M., and Kinne, S.: Dust layer effects on the atmospheric
9 radiative budget and heating rate profiles, *Atmos. Environ.*, 59, 344-354, 2012.

10 Perrone, M. R., De Tomasi, F., and Gobbi, G. P.: Vertically resolved aerosol properties
11 from multi-wavelength lidar measurements, *Atmos. Chem. Phys.* 14, 1185–1204, 2014.
12 doi:10.5194/acp-14-1185-2014

13 Seinfeld, J. H., and S. N. Pandis, S. N., *Atmospheric Chemistry and Physics: From Air*
14 *Pollution to Climate Change*, J. Wiley & Sons, INC, 1998.

15 Schuster, G. L., Dubovick, O., and Holben, B. N.: Angstrom exponent and bimodal
16 aerosol size distributions, *J. Geophys. Res.*, 111, D07207, doi:10.1029/2005/JD006328, 2006.

17 Tafuro, A. M., Kinne, S., De Tomasi, F., and Perrone, M. R.: Annual cycle of aerosol
18 direct radiative effect over southeast Italy and sensitivity studies, *J. Geophys. Res.*, 112,
19 D20202, doi:10.1029/2006JD008265, 2007.

20 Veselovskii, I., Dubovik, O., Kolgotin, A., Lapyonok, T., Di Girolamo, P., Summa, D.,
21 Whiteman, D. N., Mishchenko, M., and Tanre, D.: Application of randomly oriented spheroids
22 for retrieval of dust particle parameters from multi-wavelength lidar measurements, *J.*
23 *Geophys. Res.*, 115, D21203, doi:10.1029/2010JD014139, 2010.

24 Veselovskii, I., Dubovik, O., Kolgotin, A., Korenskiy, M., Whiteman, D. N.,
25 Allakhverdiev, and Huseynoglu, F.: Linear estimation of particle bulk parameters from multi-
26 wavelength lidar measurements, *Atmos. Meas. Tech.*, 5, 1135-1145, 2012.

27 Wagner R., Ajtai, T., Kandler, K., Lieke, K., Muller, T., Schnaiter, M., and Vragel, M.:
28 Complex refractive indices of Sahara dust samples at visible and near UV wavelengths: a
29 laboratory study, *Atm. Chem. Phys.*, 12, 2491-2512, 2012.

30 Wagner, J., Ansmann, A., Wandinger, U., Seifert, P., Schwarz, A., Tesche, M., Chaikovsky,
31 A., and Dubovik, O.: Evaluation of the Lidar/Radiometer Inversion Code (LIRIC) to determine

1 microphysical properties of volcanic and desert dust, *Atmos. Meas. Tech.*, 6, 1707–1724,
2 doi:10.5194/amt-6-1707-2013, 2013.

3

4

5

1 **Figure Captions**

2
3 **Fig.1** Aerosol classification framework calculated for mixed aerosol types (black lines) by
4 setting $n = 1.455$ and $k = 0.0047$ at 532 nm, for desert dust particles (yellow lines) by setting n
5 $= 1.55$ and $k = 0.008$ at 532 nm, and for large desert dust particles by setting the coarse modal
6 radius equal to 0.75, 0.9, 0.105, and 0.2 μm (blue lines).

7
8 **Fig.2.** (a) Vertical profiles of the fine (black) and coarse (violet) particle volume concentrations
9 with corresponding uncertainties retrieved from LIRIC by using lidar measurements performed
10 on August 29, 2011 from 13:56 to 14:27 UTC. (b) Vertical profiles of ~~(b)~~ extinction
11 coefficients at 355, 532, and 1064 nm from LIRIC (dotted lines) and the CII procedure (solid
12 lines); (c) Lidar ratio vertical profiles at 355, 532, and 1064 nm from LIRIC (dotted lines)
13 and the CII procedure (solid lines); and (d) Vertical profiles of the fine mode fractions at 355
14 nm (blue), 532 nm (green), and 1064 nm (red) from LIRIC. Error bars represent ± 1 standard
15 deviation (SD) of mean values (dotted lines) and the constrained iterative procedure (solid
16 lines) with corresponding uncertainties (error bars).

17
18 **Fig. 3** (a) Pathways estimated at 14:00 UTC of August 29, 2011, of the ten day HYSPLIT
19 backtrajectories with arrival heights at 1, 2, and 3 km a.g.l. (b) Time evolution of the altitude of
20 each backtrajectory. (c) 10-day fire map by MODIS from 20 to 29 August, 2011
21 (<http://rapidfire.sci.gsfc.nasa.gov/firemaps/>)

22
23 **Fig. 4** Vertical profiles of (a) $\mathring{A}(532, 1064, z)$ and $\mathring{A}(355, 532, z)$ by green and blue lines,
24 respectively, Angstrom exponents for different wavelength pairs and of (b) $\mathring{A}(355, 1064,$
25 $z)$ the 355-1064 nm Angstrom exponent (black lines) and of the spectral difference (red lines)
26 from LIRIC (dotted lines) and the CII constrained iterative inversion procedure (solid lines),
27 with corresponding SDs of mean values uncertainties (error bars).

28
29 **Fig. 5** ~~Solid and dashed black lines represent the~~ Graphical framework calculated for $n =$
30 1.455 and $k = 0.0047$ at 532 nm. ~~Solid lines represent the η_{GF} values at 532 nm equal to 1, 10,~~
31 ~~30, 50, 70, 90, and 99%. Dashed lines represent the R_{GF} values equal to 0.02, 0.05, 0.1, 0.15,~~
32 ~~0.20, 0.30, and 0.40 μm .~~ Open triangles ~~provide~~ represent $\Delta\mathring{A}_L(z)$ versus $\mathring{A}_L(355, 1064, z)$ mean
33 values with corresponding SDs ~~uncertainties~~ retrieved from LIRIC by using the lidar
34 measurements performed on August 29, 2011 from 13:56 to 14:27 UTC. Full dots represent
35 $\Delta\mathring{A}(z)$ versus $\mathring{A}(355, 1064, z)$ mean values obtained from the CII-procedure. Error bars
36 represent SDs of mean values ~~uncertainties~~. Different colors are used to represent spectral
37 difference and Angstrom values referring to different altitudes z , as indicated by the color bar
38 on the right of the figure.

39
40 **Fig. 6** (a) Vertical profiles of the fine (black) and coarse (violet) particle volume concentrations
41 with corresponding uncertainties retrieved from LIRIC by using lidar measurements performed
42 on September 12, 2011 from 14:06 to 14:36 UTC. (b) Vertical profiles of ~~the(b)~~ extinction
43 coefficients, at 355, 532, and 1064 nm from LIRIC (dotted lines) and the CII procedure (solid
44 lines). (c) Lidar ratio vertical profiles at 355, 532, and 1064 nm from LIRIC (dotted lines) and
45 the CII procedure (solid lines). (d) Vertical profiles of the fine mode fractions at 355, 532, and
46 1064 nm from LIRIC. Error bars represent ± 1 SD of mean values. ~~(e) lidar ratios, and (d) fine~~

Formattato: Tipo di carattere: Corsivo
Formattato: Tipo di carattere: Corsivo
Formattato: Tipo di carattere:
Corsivo, Pedice

1 ~~mode fractions at 355 nm (blue), 532 nm (green), and 1064 nm (red) from LIRIC (dotted lines)~~
2 ~~and the constrained iterative procedure (solid lines) with corresponding uncertainties (error~~
3 ~~bars).~~

4
5 **Fig. 7** Vertical profiles of (a) $\hat{A}(532, 1064, z)$ and $\hat{A}(355, 532, z)$ by green and blue lines,
6 respectively, ~~Angstrom exponents for different wavelength pairs and of (b) of $\hat{A}(355, 1064,$~~
7 ~~$z)$ the 355–1064 nm Angstrom exponent (black lines) and $\Delta\hat{A}(z)$ of the spectral difference (red~~
8 ~~lines) from LIRIC (dotted lines) and the CII constrained iterative inversion procedure (solid~~
9 ~~lines) with corresponding SDs of mean values uncertainties (error bars).~~

10
11 **Fig. 8** (a) Pathways estimated at 14:00 UTC of September 12, 2011, of the seven day
12 HYSPLIT backtrajectories with arrival heights at 0.5, 1.5, and 2.5 km a.g.l. (b) Time evolution
13 of the altitude of each backtrajectory.

14
15
16 **Fig. 9** Solid and dashed black lines represent the graphical framework calculated for $n = 1.455$
17 and $k = 0.0047$ at 532 nm. Open triangles represent $\Delta\hat{A}_L(z)$ versus $\hat{A}_L(355, 1064, z)$ values
18 with corresponding ~~SDs uncertainties~~ retrieved from LIRIC by using the lidar measurements
19 performed on September 12, 2011 from 14:06 to 14:36 UTC. Full dots represent $\Delta\hat{A}(z)$ versus
20 $\hat{A}(355, 1064, z)$ values from the CII-procedure. Error bars represent SDs of mean
21 values uncertainties. Different colors are used to represent values referring to different altitudes
22 z , as indicated by the color bar on the right of the figure.

23
24 **Fig. 10** Vertical profile of the linear particle depolarization ratio (black line) with
25 corresponding uncertainties (error bars) retrieved from lidar measurements performed on
26 August 6, 2012 from 14:57 to 15:21 UTC, and of the dust mass concentration (red line)
27 simulated by the BSC-DREAM at 12:00 UTC of August 6, 2012.

28
29 **Fig. 11** (a) Pathways estimated at 15:00 UTC of August 6, 2012, of the ten day HYSPLIT
30 backtrajectories with arrival heights at 1, 2.5 and 4.5 km a.g.l.. (b) Time evolution of the
31 altitude of each backtrajectory.

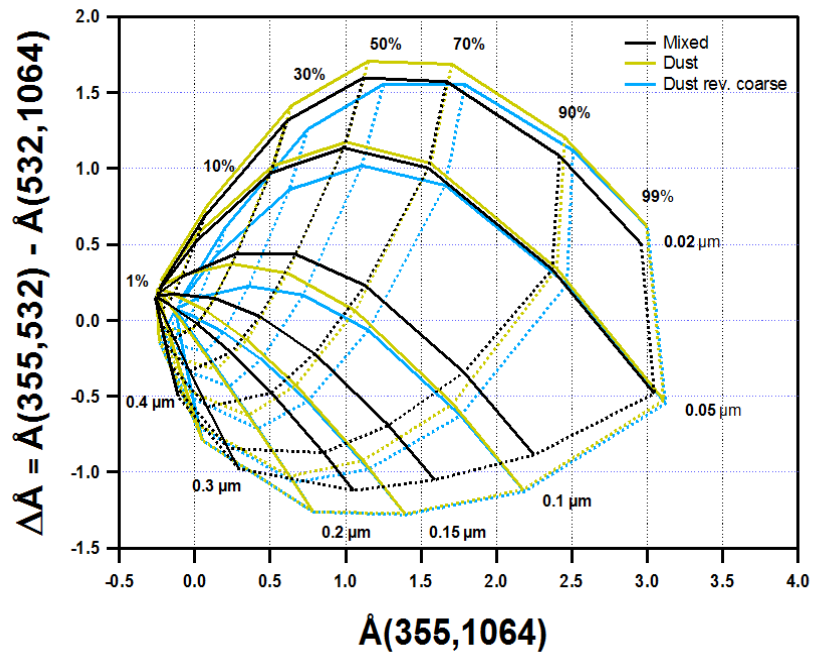
32
33 **Fig. 12** (a) Vertical profiles of the fine (black dotted line) and coarse (violet dotted line)
34 particle volume concentrations with corresponding uncertainties retrieved from LIRIC by using
35 lidar measurements performed on August 6, 2012 from 14:57 to 15:21 UTC. (b) Vertical
36 profiles of ~~(b) the~~ extinction coefficients at 355, 532, and 1064 nm from LIRIC (dotted lines)
37 and the CII procedure (solid lines). (c) Lidar ratio vertical profiles at 355, 532, and 1064 nm
38 from LIRIC (dotted lines) and the CII procedure (solid lines). (d) Vertical profiles of the fine
39 mode fractions at 355, 532, and 1064 nm from LIRIC. Error bars represent ± 1 SD of mean
40 values.; (e) lidar ratios, and (d) fine mode fractions at 355 nm (blue), 532 nm (green), and 1064
41 nm (red) from LIRIC (dotted lines) and the constrained iterative procedure (solid lines) with
42 corresponding uncertainties (error bars).

43
44 **Fig. 13** Vertical profiles of the potential temperature (θ) and relative humidity (RH) retrieved
45 from radio sounding measurements performed on August 6 at 11:00 UTC.

46

1 **Fig. 14** Vertical profiles of (a) $\mathring{A}(532, 1064, z)$ and $\mathring{A}(355, 532, z)$ by green and blue lines,
2 respectively, ~~Angstrom exponents for different wavelength pairs~~ and of (b) of $\mathring{A}(355, 1064,$
3 ~~z) the 355–1064 nm Angstrom exponent~~ (black lines) and $\Delta\mathring{A}(z)$ of the spectral difference (red
4 lines) from LIRIC (dotted lines) and the ~~CII constrained iterative inversion procedure~~ (solid
5 lines) with corresponding ~~SDs of mean values~~ ~~uncertainties~~ (error bars).
6

7 **Fig. 15** Solid and dashed black lines represent the graphical framework calculated for $n = 1.55$
8 and $k = 0.008$ at 532 nm and coarse mode radii $R_{c,GF} = 0.75, 0.9, 0.105,$ and $0.12 \mu\text{m}$ (Dust-rev
9 framework). Open triangles represent $\Delta\mathring{A}_L(z)$ versus $\mathring{A}_L(355, 1064, z)$ values with
10 corresponding ~~SDs~~ ~~uncertainties~~ from LIRIC by using the lidar measurements performed on
11 September 12, 2011 from 14:06 to 14:36 UTC. Full dots represent $\Delta\mathring{A}(z)$ versus $\mathring{A}(355, 1064,$
12 $z)$ values. Error bars represent ~~SDs of mean values~~ ~~uncertainties~~. Different colors are used to
13 represent values referring to different z , as indicated by the ~~figthright~~ of the
14 figure.
15
16
17



1
2
3
4
5
6

Figure 1 (M. R. Perrone)

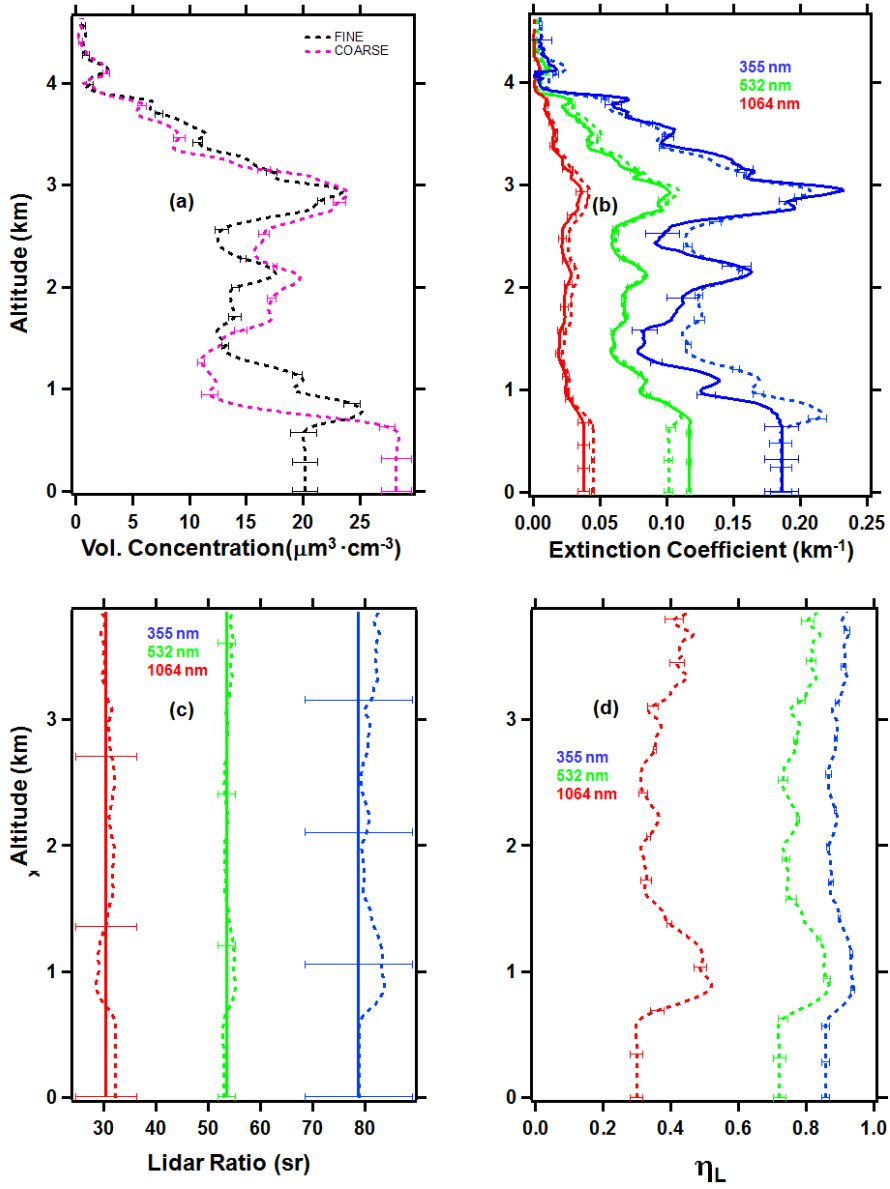


Figure 2 (M. R. Perrone)

1
2
3
4
5
6

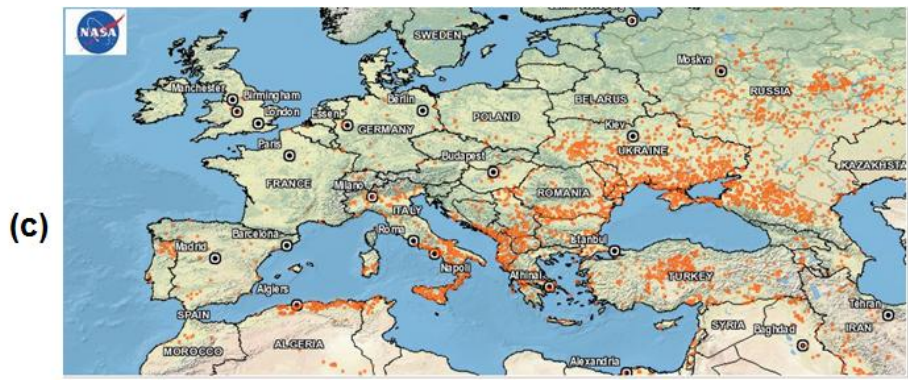
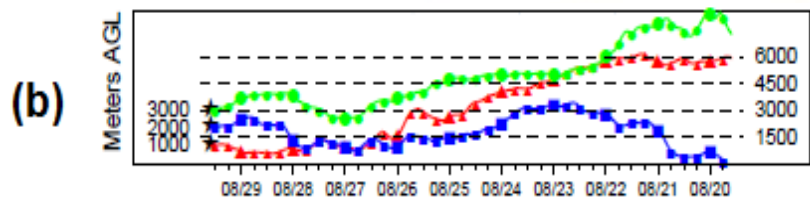
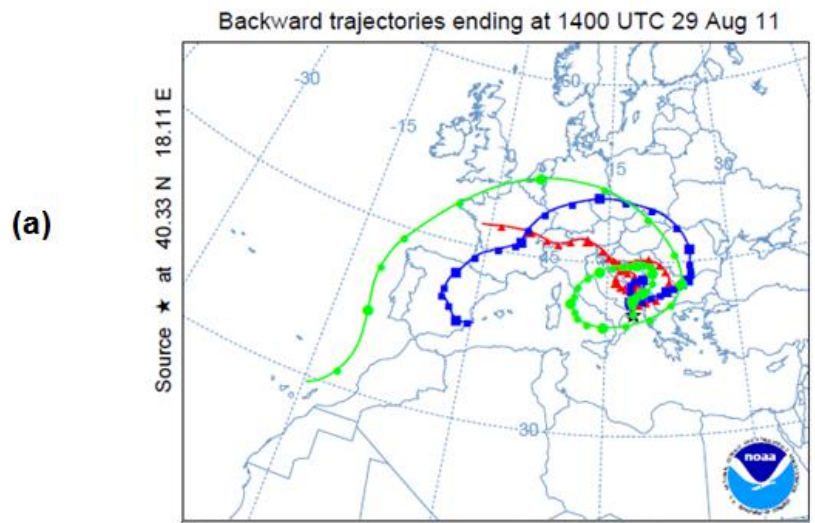


Figure 3 (M. R. Perrone)

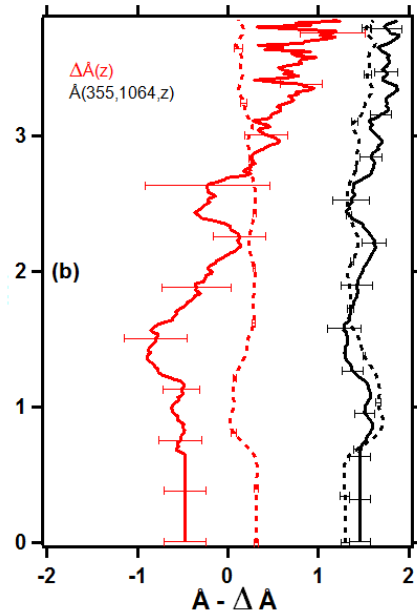
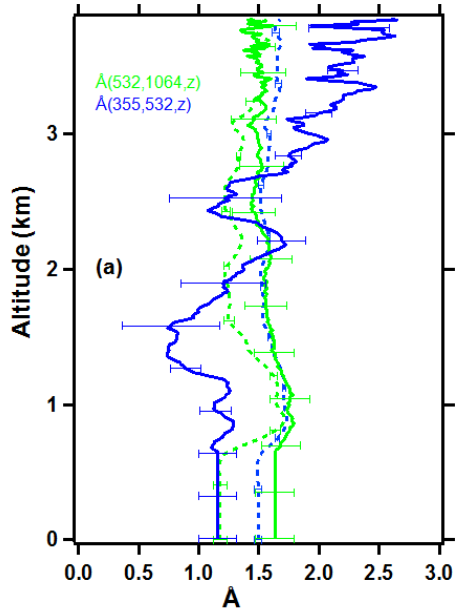
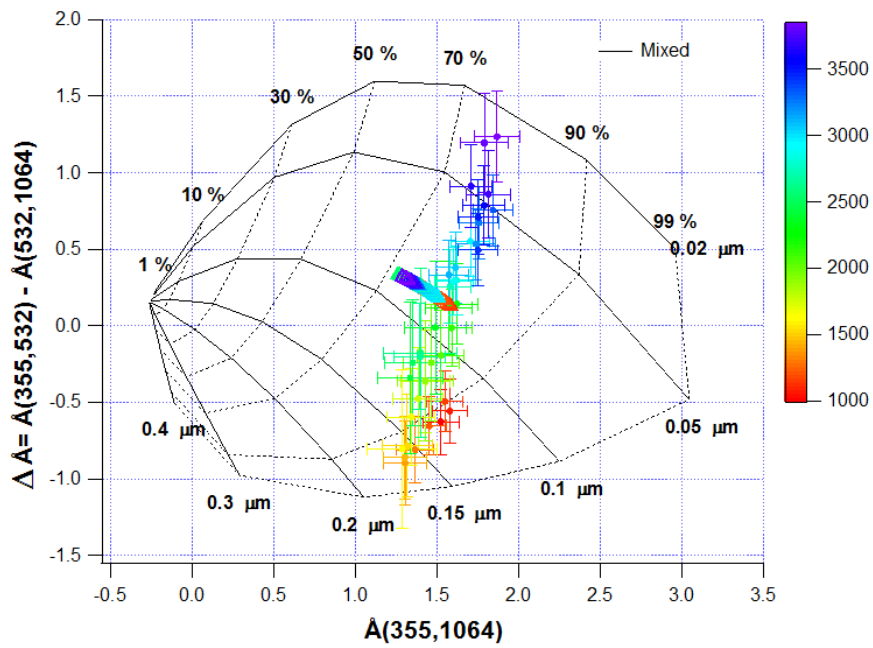


Figure 4 (M.R. Perrone)

1
2
3
4
5
6
7
8
9



1
2
3
4
5
6
7

Figure 5 (M.R. Perrone)

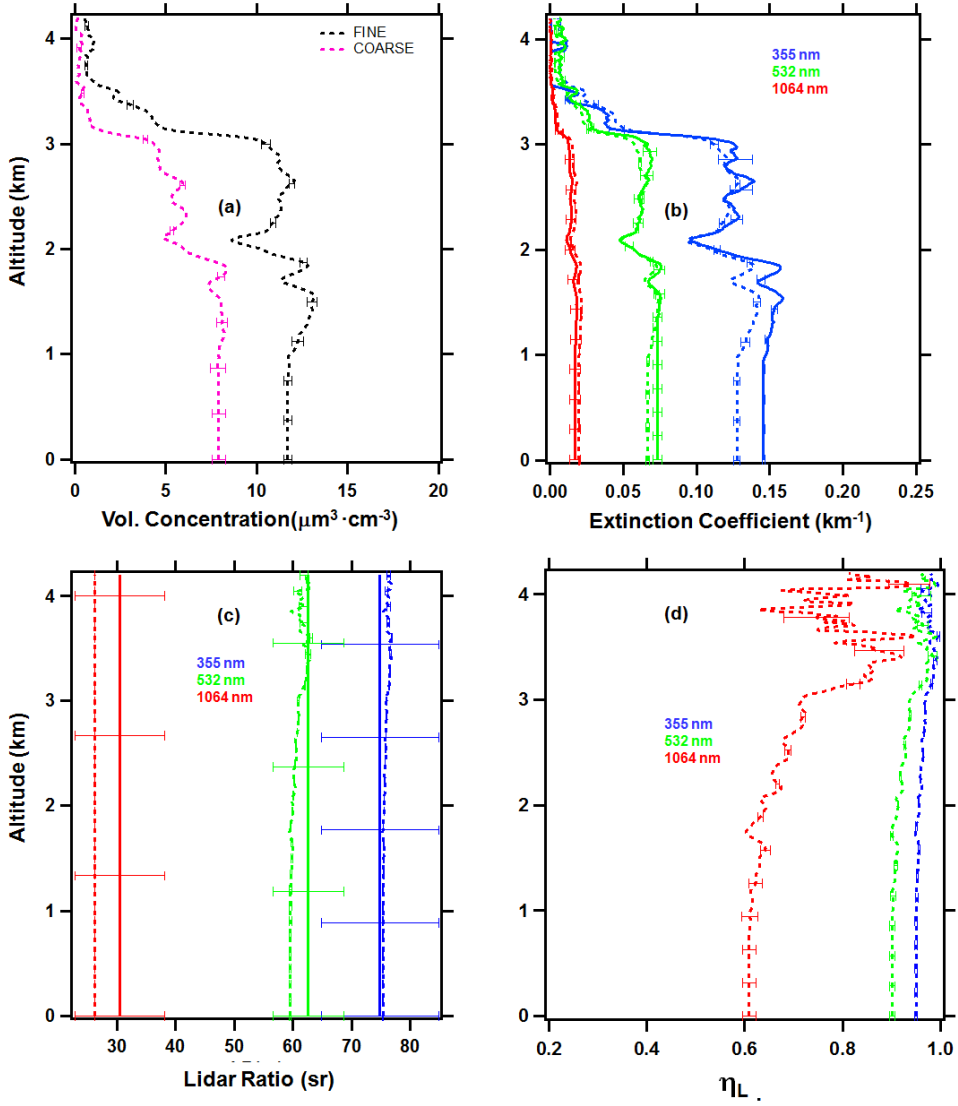
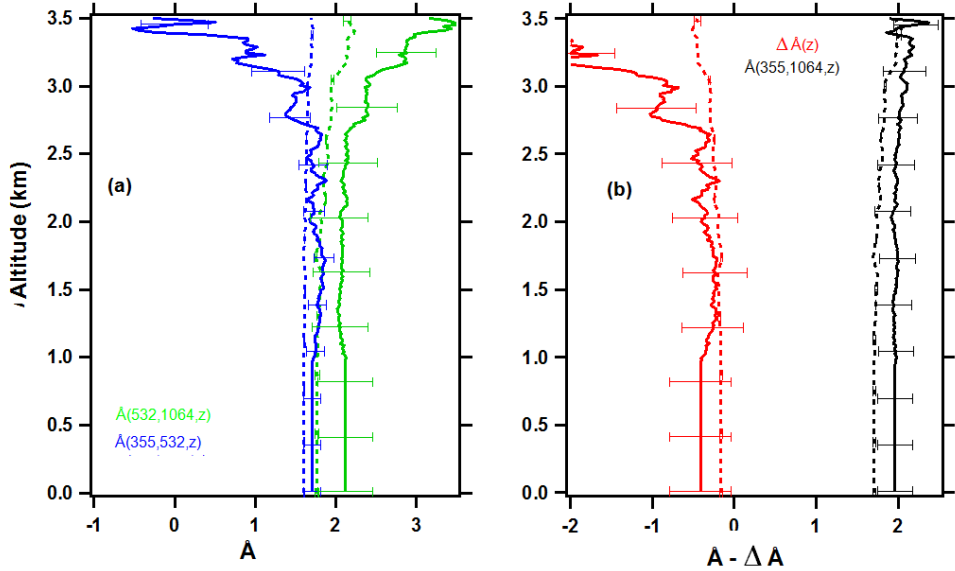


Figure 6 (M. R. Perrone)

1
2
3
4
5
6
7
8



1
2
3
4
5
6
7
8
9

Figure 7 (M.R. Perrone)

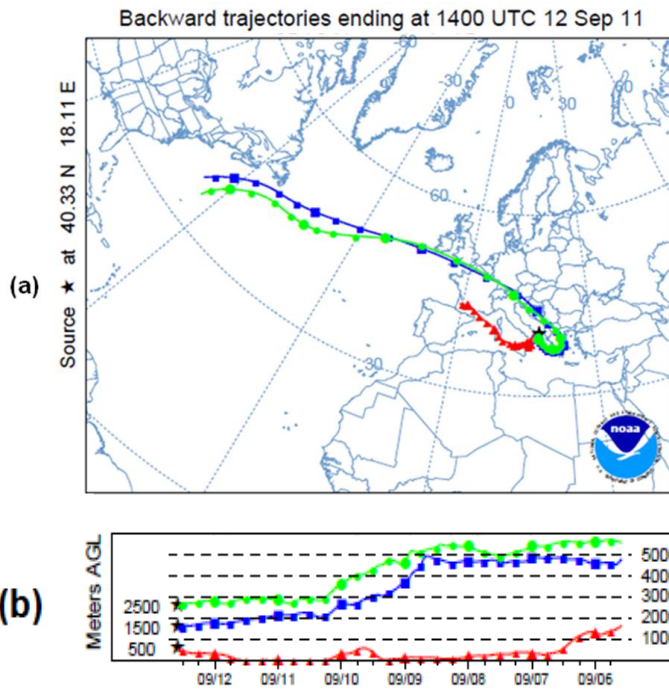
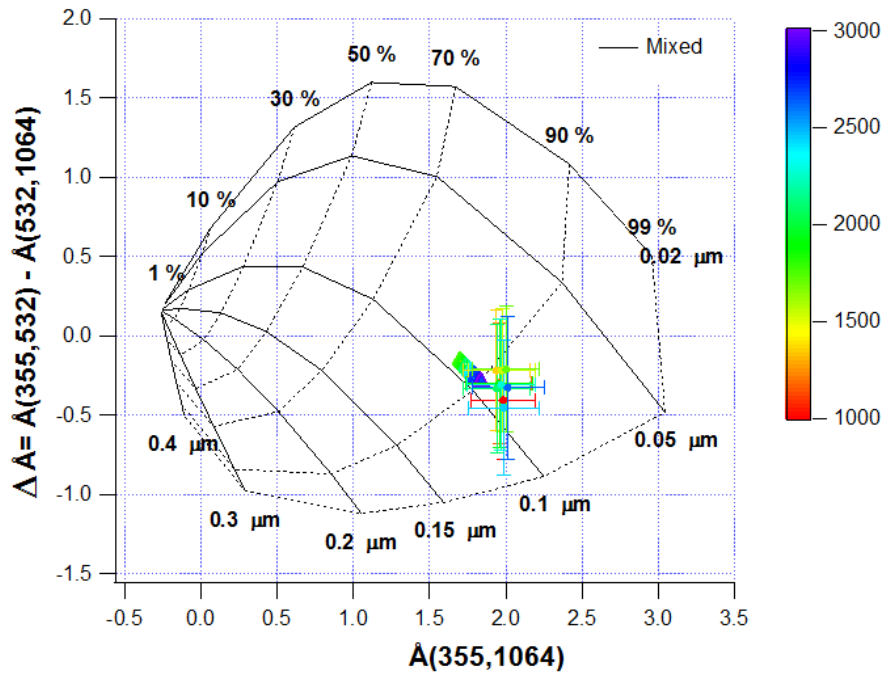


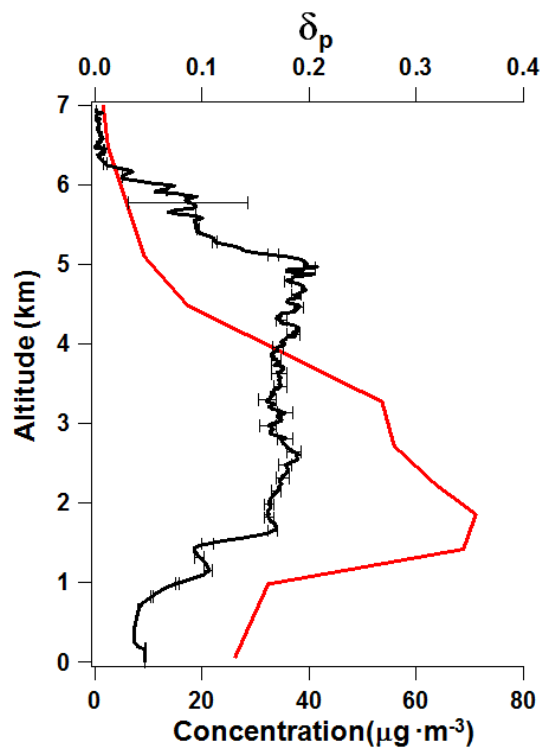
Figure 8 (M. R. Perrone)

1
2
3
4
5
6
7
8
9
10
11



1
2
3
4
5
6
7
8

Figure 9 (M. R. Perrone)



1
2
3
4
5
6
7

Figure 10 (M. R. Perrone)

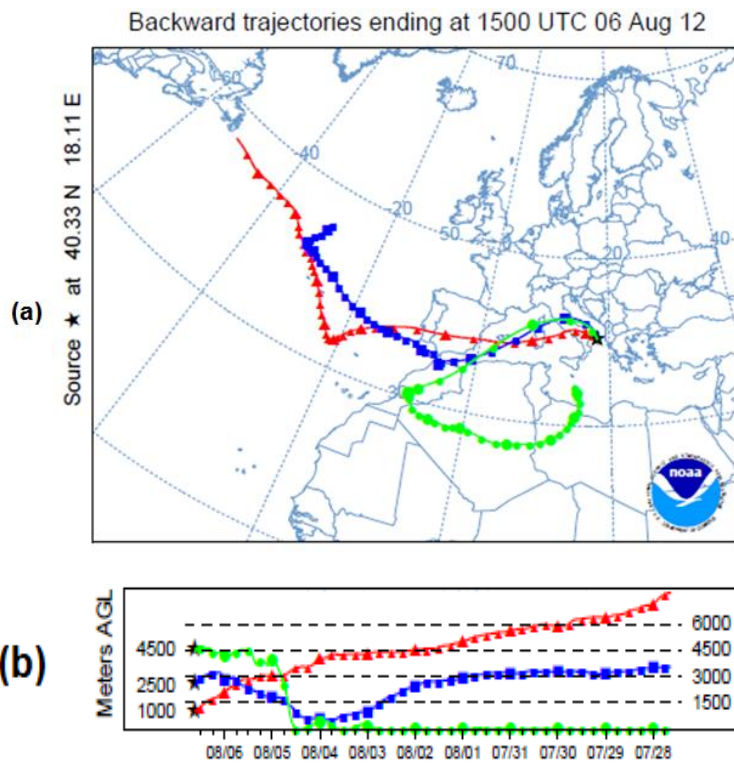


Figure 11 (M.R. Perrone)

1
2

3
4
5
6
7
8
9
10

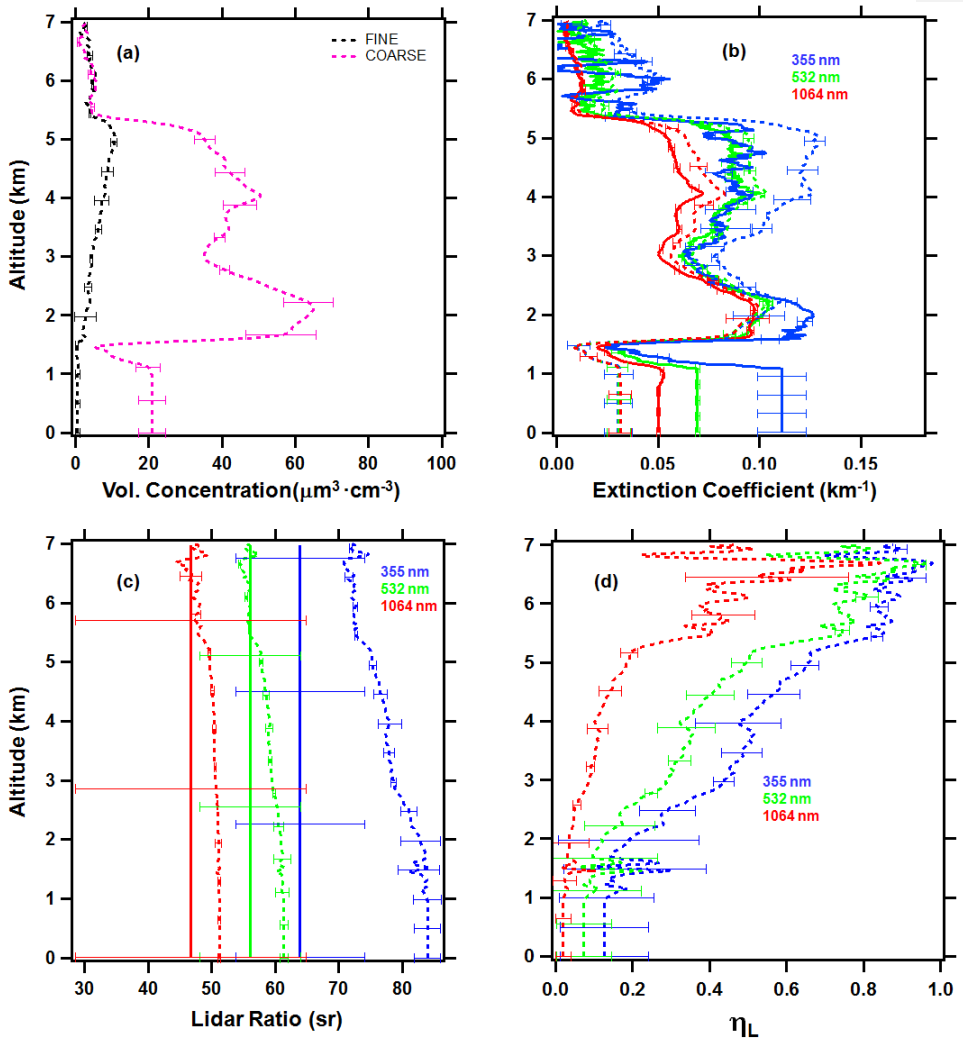


Figure 12 (M. R. Perrone)

1
2
3
4
5
6
7
8

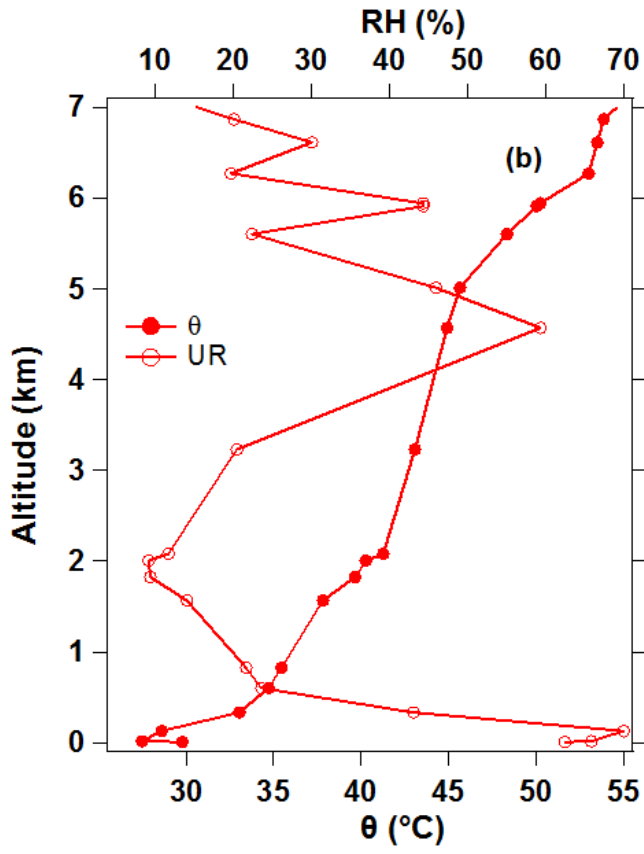


Figure 13 (M. R. Perrone)

1
2
3
4
5
6
7
8
9

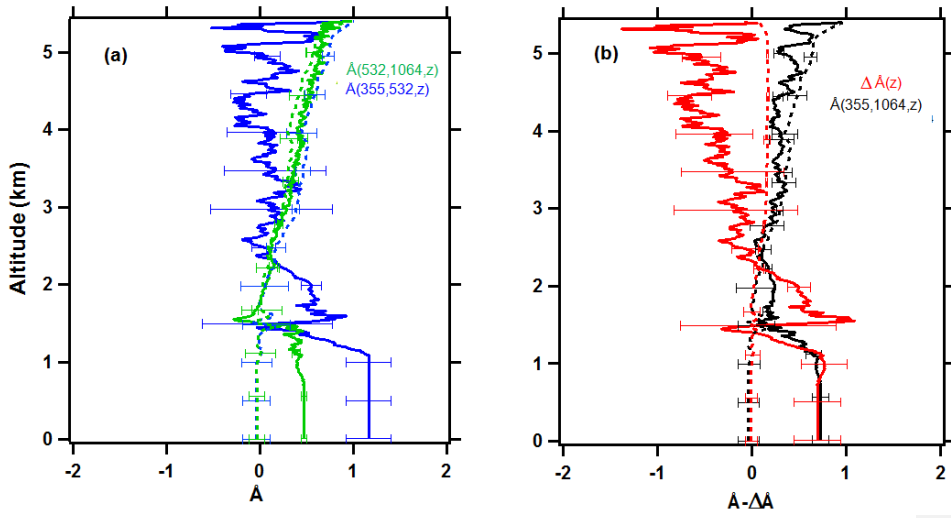
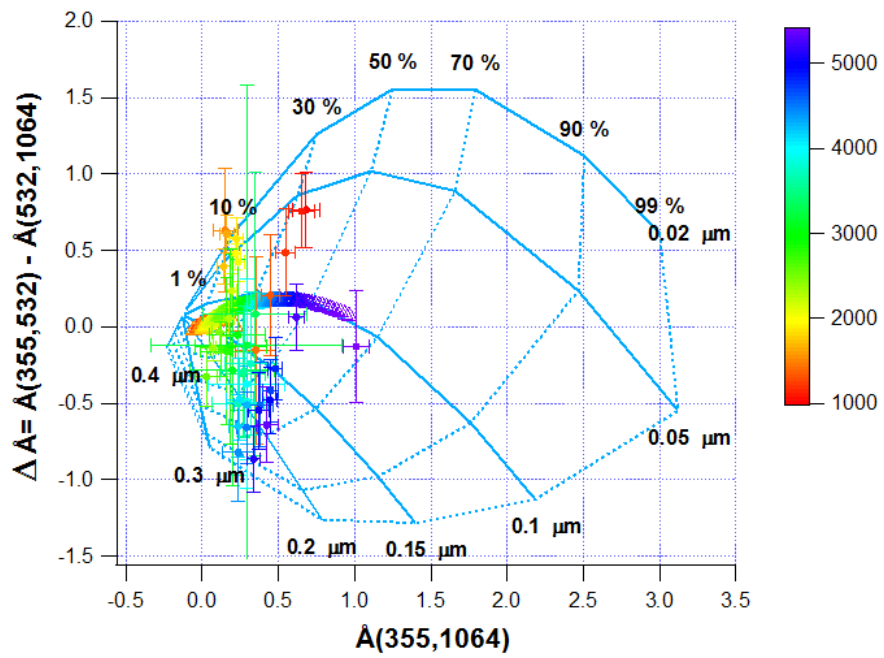


Figure 14 (M. R. Perrone)

1
2
3
4
5
6
7
8



1
2
3
4
5
6

Figure 15 (M. R. Perrone)